s

Experimental validation of the hybrid scattering model of installed jet noise

Benshuai Lyu[1, a)] and Ann Dowling[1]

Department of Engineering, University of Cambridge

(Dated: 1 August 2018)

Jet installation causes jet noise to be amplified significantly at low frequencies and its physical mechanism must be understood to develop effective aircraft noise reduction strategies. A hybrid semi-empirical prediction model has recently been developed based on the instability-wave-scattering mechanism. However, its validity and accuracy remain to be tested. To do so, in this paper we carry out a systematic installed jet-noise experiment in the laboratory using a flat plate instead of an aircraft wing. We show that reducing H (the separation distance between the flat plate and jet centreline) causes stronger low-frequency noise enhancement while resulting in little change to the noise shielding and enhancement at high frequencies. Decreasing L (the axial distance between the jet exit plane and the trailing edge of the plate) results in reduced noise amplification at low frequencies and also weakens both the shielding and enhancement at high frequencies. Increasing the jet Mach number abates the installation effects. It is shown that the hybrid model developed in the earlier work agrees with experimental measurements and can capture the effects of varying H, L and jet Mach number extremely well. It is concluded that the model captures the correct physics and can serve as an accurate and robust prediction tool. This new physical understanding provides insights into innovative strategies for suppressing installed jet noise.

a)bl362@cam.ac.uk

I. INTRODUCTION

The International Civil Aviation Organization (ICAO), a UN specialized agency, reports that the global air transportation network doubles every 15 years, and this trend is expected to continue by 2030. Currently, there are more than 100000 daily flights in this global network. This existing large fleet and its foreseeable rapid increase raise concerns for their significant impact on the environment. One great concern is the noise disturbance that it causes. Since aircraft noise appeared on the agenda, extensive research has been carried out to reduce it.

Among the many components of aircraft noise, jet noise still dominates at take-off. In modern aircraft, however, the aero-engines are installed very close to the aircraft wings, and jet noise is modified significantly by the wings and other high lift devices. This modified jet noise is commonly called installed jet noise, in comparison with the isolated jet noise. Installed jet noise is significantly louder than isolated jet noise at low frequencies. To reduce aircraft noise, it is therefore necessary to understand how and why noise is intensified at these low frequencies in the installed case.

Research on installed jet noise dates back a few decades and the early research was mostly experimental work. The low-frequency sound intensification due to jet installation effects was noted by Bushell [1] in 1975 in his full-scale flight tests. A systematic model-scale experimental investigation was conducted by Head and Fisher [2] the following year. They concluded that the installed noise source has a dipole directivity and that the noise intensity depends on the sixth power of the jet exit velocity. These installation effects were further examined and confirmed by the experiments of Szewczyk,[3] Way and Turner [4] and Shearin [5] in 1979, 1980 and 1983 respectively.

Noise prediction models and reduction strategies were also attempted in the early 1980s. The works of Stevens, Bryce, and Szewczyk [6] and Sengupta [7] represented two early attempts in developing prediction models for installed jet noise. The former achieved this by summing up jet noise and core noise measured for a model-scale aircraft, while the latter proposed numerically fitted models based also on the data from experimental tests. The experiment of Wang [8] investigated the noise reduction feasibility of using aircraft wings with different acoustic surface properties. However, it was found that the noise reduction occurred mainly at high frequencies, while the installed jet noise is mainly relevant at low frequencies.

There were few research activities in the late 1980s and early 1990s. This completely changed in 1998, when Mead and Strange [9] conducted experiments which aimed to understand the installation effects for sideline observers. In the same year, Bhat and Blackner [10] proposed an empirically-fitted noise prediction model. However, attempts to account for the installation were rather empirical. The work of Moore [11] was somewhat less so. He/she used a model based on 3D ray theory to quantify the acoustic propagation effects. A few years

later, Pastouchenko and Tam[12] were among the first to study the jet installation effects using a Computational Fluid Dynamics (CFD) method. Based on their numerical results, they claimed it was the downwash of jet mean flow that caused the noise enhancement.

Research interest has been continuously growing since 2012. This is partly because the engine bypass ratios and jet diameters continue to increase, causing the jet installation effects to became increasingly pronounced. While Brown's[13] measurement added to the experimental database of installed jet noise, the research focus during this period has been on developing predictive models. Similar to the approach used by Papamoschou,[14] Cavalieri *et al.*[15] proposed a wave-packet scattering model, and the far-field sound was calculated using a numerical Green's function integration and a Boundary Elemment Method (BEM). The same two modelling strategies were used by Piantanida *et al.*[16] to model the installed jet noise from aircraft wings with swept trailing edges. In both studies, a good overall agreement for the noise directivity was observed at a few discrete frequencies. On the other hand, Vera, Self, and Kingan[17] examined the scattering problem by a different method – they used Amiet's approach.[18] However, the results, as they noted in their paper, were not particularly convenient for quantifying noise sources because they are not statistically stationary.

Following Piantanida *et al.*,[19] the idea of using swept aircraft wings to reduce installed jet noise was further explored by Nogueira, Cavalieri, and Jordan.[20] As an other attempt, Bastos, Deschamps, and da Silva[21] investigated the effects of chevron nozzles on installed jet noise. They found that the installed jet noise was not sensitive to the chevron geometries when the aircraft wing was close to the jet, though an overall slight noise reduction could be achieved when they were away from each other.

In the recent works of the authors,[22,23] a hybrid prediction model was developed to account for the installation effects. The model consists of contributions from both the scattering of Lighthill's quadrupole sources and the scattering of near-field instability waves by the trailing edge of the aircraft wing. It is found that the scattering of jet instability waves accounts for the low-frequency enhancement observed in experiments. In contrast, at high frequencies, noise is either reduced on the shielded side or enhanced by around 3 dB on the reflected side of the plate in accord with classical acoustic scattering theories. The model agrees well with the data from early experimental tests.[2]

As a continuation of this research, in this paper, we carry out an experimental investigation. One of the aims of this experimental study is to advance our understanding of the characteristics of installed jet noise and the near-field pressure fluctuations (due to jet instability waves), as an aid to developing noise controlling strategies. The other aim is to further validate the hybrid prediction model developed in the earlier work of the authors[22,23] by obtaining a comprehensive experimental database. In particular, the hybrid model developed in those works requires the power spectral densities of the near-field pressure fluctuations as

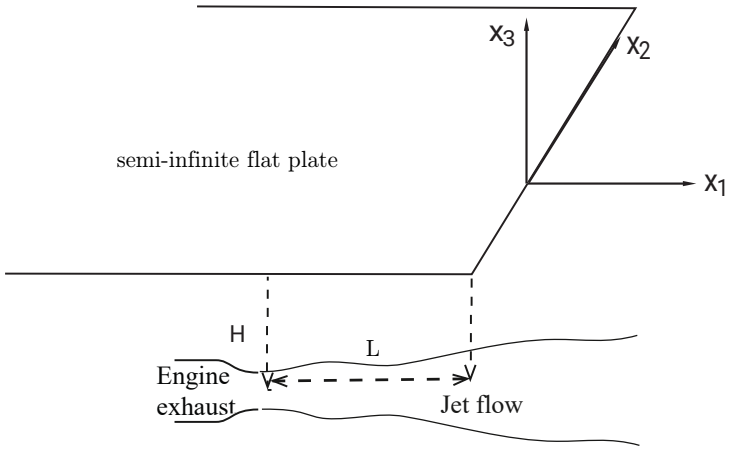

FIG. 1: Schematic of the simplified model with a semi-infinite flat plate.

an input. In experiments, we measure such information specifically for the model. In what follows, we first briefly review the hybrid model, then describe the experimental setup. The experimental results then follow. The next section shows the comparison of the experimental results with model predictions, and the conclusions of the paper are presented subsequently.

II. THE HYBRID PREDICTION MODEL

As mentioned in section I, the model developed in the earlier work of the authors[23] consists of two parts, i.e., the total sound power spectral density

$$\Phi(\omega, \boldsymbol{x}) = \Phi_Q(\omega, \boldsymbol{x}) + \Phi_N(\omega, \boldsymbol{x}), \tag{1}$$

where $\Phi_Q(\omega, \boldsymbol{x})$ denotes the power spectrum due to Lighthill's quadrupole sources and $\Phi_N(\omega, \boldsymbol{x})$ denotes the contribution due to the near-field instability wave scattering. The model starts by simplifying the wing into a semi-infinite flat plate, as shown in figure 1. The plate is also infinite in the spanwise direction so that no side-edges are present. x_1, x_2 and x_3 denote the axes in the streamwise, spanwise and perpendicular directions respectively. L is the horizontal distance between the jet nozzle and the trailing edge of the flat plate, while H represents the separation distance between the jet centerline and the bottom surface of the plate.

A. Quadrupole scattering

The first part of the model makes use of Lighthill's acoustic analogy theory using a half-plane scattering Green's function $G(\boldsymbol{x}; \boldsymbol{y}, \omega)$. The details of this function were outlined in an earlier paper.[23] The far-field power spectral density due to these quadrupole sources,

$\Phi_Q(\boldsymbol{x},\omega)$, is given by

$$\Phi_Q(\boldsymbol{x},\omega) = c_0^4 \int_{V_y} \int_{V_{\Delta y}} R_{ijkl}(\boldsymbol{y},\Delta\boldsymbol{y},\omega) I_{ijkl}(\boldsymbol{x},\boldsymbol{y},\Delta\boldsymbol{y},\omega)\,\mathrm{d}^3\Delta y\,\mathrm{d}^3 y, \tag{2}$$

where c_0 denotes the speed of sound in fluid and

$$\begin{aligned} R_{ijkl}(\boldsymbol{y},\Delta\boldsymbol{y},\omega) &= \int \overline{T_{ij}(\boldsymbol{y},t)T_{kl}(\boldsymbol{y}+\Delta\boldsymbol{y},t+\tau)}\frac{\mathrm{e}^{-\mathrm{i}\omega\tau}}{2\pi}\,\mathrm{d}\tau, \\ I_{ijkl}(\boldsymbol{x},\boldsymbol{y},\Delta\boldsymbol{y},\omega) &= \frac{\partial^2 G(\boldsymbol{x};\,\boldsymbol{y},\omega)}{\partial y_i \partial y_j}\frac{\partial^2 G^*(\boldsymbol{x};\,\boldsymbol{y}+\Delta\boldsymbol{y},\omega)}{\partial y_k \partial y_l}. \end{aligned} \tag{3}$$

T_{ij} in the above equation is Lighthill's stress tensor (see more in Lyu, Dowling, and Naqavi [23]).

The fourth-order space-time correlation function $R_{ijkl}(\boldsymbol{y},\Delta\boldsymbol{y},\tau)$ describes the quadrupole sources and can be modelled well using a Gaussian function as[24]

$$\begin{aligned} R_{ijkl}(\boldsymbol{y},\Delta\boldsymbol{y},\tau) = A_{ijkl}(\boldsymbol{y}) \exp\Bigg[&-\frac{|\Delta y_1|}{\bar{u}_1(\boldsymbol{y})\tau_s(\boldsymbol{y})} \\ &- \ln 2 \left(\left(\frac{\Delta y_1 - \bar{u}_1(\boldsymbol{y})\tau}{l_1(\boldsymbol{y})} \right)^2 + \left(\frac{\Delta y_2}{l_2(\boldsymbol{y})} \right)^2 + \left(\frac{\Delta y_3}{l_3(\boldsymbol{y})} \right)^2 \right) \Bigg], \end{aligned} \tag{4}$$

where $A_{ijkl}(\boldsymbol{y}) = C_{ijkl}(2\bar{\rho}k)^2$, $l_i = c_i k^{3/2}/\epsilon$ and $\tau_s = c_\tau k/\epsilon$. Here $\bar{\rho}$ is the time-averaged fluid density, $\bar{u}_1$ represents the averaged streamwise velocity, k is the turbulence kinetic energy, ϵ denotes the turbulent dissipation rate. These time-averaged quantities can be calculated using RANS simulation. The constants C_{ijkl}, c_i and c_τ can be obtained by fitting equation 4 to the space-time correlation data obtained from Large Eddy Simulations (LES). We used the constants found in the previous work,[23] i.e. c_1, c_2, c_3, c_τ are taken to be around 0.4, 0.23, 0.23, 0.3 respectively, which are close to those obtained by Karabasov *et al.*,[24] but also account for the anisotropy of the turbulence length scales (see Mohan *et al.*[25]). C_{ijkl} remain the same as those found by Karabasov *et al.*.[24] Equation 4 is known to be able to model the fourth-order space-time correlation well, though it does not account for the cusp behavior at short time delays.[24,25] Such a model should also suffice for installed jet noise, provided that the flat plate is not so close to the jet as to change the flow considerably. Using equation 4, the cross-spectra is thus obtained by performing the standard Fourier transformation, which yields

$$\begin{aligned} R_{ijkl}(\boldsymbol{y},\Delta\boldsymbol{y},\omega) = &\frac{l_1(\boldsymbol{y})}{2\bar{u}_1(\boldsymbol{y})\sqrt{\pi \ln 2}} A_{ijkl}(\boldsymbol{y}) \exp\left[-\frac{l_1(\boldsymbol{y})^2\omega^2}{4\bar{u}_1^2(\boldsymbol{y})\ln 2} \right] \\ &\exp\left[-\frac{|\Delta y_1|}{\bar{u}_1(\boldsymbol{y})\tau_s(\boldsymbol{y})} - \mathrm{i}\frac{\omega}{\bar{u}_1(\boldsymbol{y})}\Delta y_1 - \ln 2 \left(\left(\frac{\Delta y_2}{l_2(\boldsymbol{y})} \right)^2 + \left(\frac{\Delta y_3}{l_3(\boldsymbol{y})} \right)^2 \right) \right]. \end{aligned} \tag{5}$$

The tensor $I_{ijkl}(\boldsymbol{x},\boldsymbol{y},\Delta\boldsymbol{y},\omega)$ in equation 3 depends solely on the Green's function. Consequently, substituting the free-space Green's function or the one accounting for half-plane

scattering into equation 2 yields results for an isolated jet or installed jet respectively. Note that this part of the scattering model does not include the refraction effects of the jet mean flow on the quadrupole sources. This is partially because we wish to obtain a Green's function of an analytical function, and including the shear-flow would make this unlikely to be possible. Detailed discussion on this can be found in the original paper.[23]

B. Instability scattering

The second part of the model accounts for the near-field instability scattering. The contribution of this mechanism to the far-field sound power spectrum, $\Phi_N(\omega, \boldsymbol{x})$, is given by[23]

$$\Phi_N(\omega,\boldsymbol{x}) = \frac{1}{\pi}\left[\frac{\omega x_3}{c_0 S_0^2}\right]^2 \sum_{m=-N}^{N}\left|\frac{\Gamma(c,\mu|_{k_2=k\frac{x_2}{S_0}},\mu_A)}{\mu_A}\right|^2 \Pi(\omega,m)$$
$$\times\left\{\sum_{k=0}^{[\frac{|m|}{2}]} C_{|m|}^{2k} H^{-2k+\frac{1}{2}}\gamma_c^{-|m|}\frac{d^{2k}}{dk_2^{2k}}\left[(\gamma_c^2+k_2^2)^{\frac{1}{2}|m|-\frac{1}{4}}K_{|m|-\frac{1}{2}}\left(H\sqrt{\gamma_c^2+k_2^2}\right)\right] -\right.$$
$$\left.\operatorname{sgn}(m)\sum_{k=0}^{[\frac{|m|-1}{2}]} C_{|m|}^{2k+1} H^{-2k+\frac{1}{2}}\gamma_c^{-|m|}\frac{d^{2k}}{dk_2^{2k}}\left[k_2(\gamma_c^2+k_2^2)^{\frac{1}{2}|m|-\frac{3}{4}}K_{|m|-\frac{3}{2}}\left(H\sqrt{\gamma_c^2+k_2^2}\right)\right]\right\}^2_{k_2=\frac{kx_2}{S0}}, \quad (6)$$

where c denotes the chord length of the plate, (x_1, x_2, x_3) denotes the Cartesian coordinates of the observer location, the stretched distance of $S_0 = \sqrt{x_1^2+\beta^2(x_2^2+x_3^2)}$, N is the largest number of azimuthal modes that we need to include, $\Pi(\omega, m)$ denotes the m-th near-field pressure power spectral density, the convective radial decay rate is given by $\gamma_c = \sqrt{(k_1\beta^2+kM)^2-k^2}/\beta$, K_i denotes the i-th modified Bessel function of the second kind, $\operatorname{sgn}(m)$ is the sign function, $[x]$ denotes the integer not larger than x, C_m^n represents the binomial coefficient and Γ is defined by

$$\begin{aligned}\Gamma(x,\mu,\mu_A) &= \mathrm{e}^{\mathrm{i}\mu_A x}E_0(\mu x)\\ &\quad -\sqrt{\frac{\mu}{\mu-\mu_A}}E_0\left[(\mu-\mu_A)x\right] - \frac{1}{1+\mathrm{i}}\mathrm{e}^{\mathrm{i}\mu_A x},\end{aligned} \quad (7)$$

where

$$\begin{aligned}\mu &= k_1 + \sqrt{k^2-k_2^2\beta^2}/\beta^2 + kM/\beta^2,\\ \mu_A &= k_1 + \frac{k}{\beta^2}(M-\frac{x_1}{S_0}),\\ E_0(x) &= \int_0^x \frac{\mathrm{e}^{-\mathrm{i}t}}{\sqrt{2\pi t}}\,\mathrm{d}t.\end{aligned} \quad (8)$$

Note that although figure 1 shows a semi-infinite flat plate, the near-field scattering model can partially capture the effects of the finite dimensions of the plate using Amiet's approach.[18] Hence $\Phi_N(\omega, \boldsymbol{x})$ also depends on c as shown in equation 6. In the definition of equations 6 and 8, M denotes the Mach number of the ambient flow while $\beta = \sqrt{1-M^2}$, k (not to be confused with the turbulence kinetic energy) denotes the acoustic wavenumber while k_1 and k_2 denote the hydrodynamic wavenumbers of the near-field pressure in the streamwise and spanwise directions respectively.

Equation 6 is the generic form of near-field scattering model. However, further simplifications can be made in practical cases. For example, if we assume that the fluctuation is symmetric with respect to the mode number m, i.e. $\Pi(\omega, m) = \Pi(\omega, -m)$, and let $\Pi_s(\omega, m) = \Pi(\omega, m) + \Pi(\omega, -m)$ for $m \neq 0$, and only two modes need to be kept, we can show the far-field sound spectral density in the mid-span plane ($x_2 = 0$) is

$$\Phi_N(\omega, \boldsymbol{x}) \approx \left[\frac{\omega x_3}{c_0 S_0^2}\right]^2 \left\{ \left| \frac{\Gamma(c, \mu, \mu_A)}{\mu_A} \right|^2 \frac{\mathrm{e}^{-2H\gamma_c}}{2\gamma_c^2} \times \left(\frac{\Pi_0(\omega, 0)}{K_0^2(\gamma_c r_0)} + \frac{\Pi_0(\omega, 1)}{K_1^2(\gamma_c r_0)} \right) \right\}_{k_2=0, U_c=\overline{U}_c(\omega)}, \tag{9}$$

where $\Pi_0(\omega, m)$ is the m-th single-sided spectrum of the incident near-field evanescent instability waves measured at $r = r_0$ and U_c is the convection velocity of the near-field instability waves. To ensure acoustic fluctuations are negligible, one can choose r_0 to be small such that the microphone is sufficiently close to the jet (but not too close to touch the jet plume). Both $\Pi_0(\omega, 0)$ and $\Pi_0(\omega, 1)$ can be obtained from experiments or LES. In this study, we use experimental results. Since these spectra vary with axial position, it makes more sense to put the microphone at the position where the trailing edge of the flat plate would be if a flat plate were present, i.e., the place where the incident wave is to be scattered. Also used in this paper is the frequency-dependent convection velocity $\overline{U}_c(\omega)$ obtained from LES studies,[23] whose validity will be verified in section VI.

III. EXPERIMENTAL SETUP

The schematic illustration of the experiment is shown in figure 2. The experimental rig is placed inside the anechoic chamber at the Engineering Department of the University of Cambridge, as shown in figures 3a and 3b. The jet nozzle has a diameter $D = 2.54$ cm. The chamber has a lowest operation frequency of around 200 Hz. As shown in figure 2, 7 GRAS 46BE microphones are placed at $50D$ to the centre of the jet nozzle, at angles in the range of $\theta = 30^\circ$ and 120° to the jet centreline. These microphones have a flat frequency response curve up to 80 kHz. The electrical signals from these 7 microphones are conditioned,

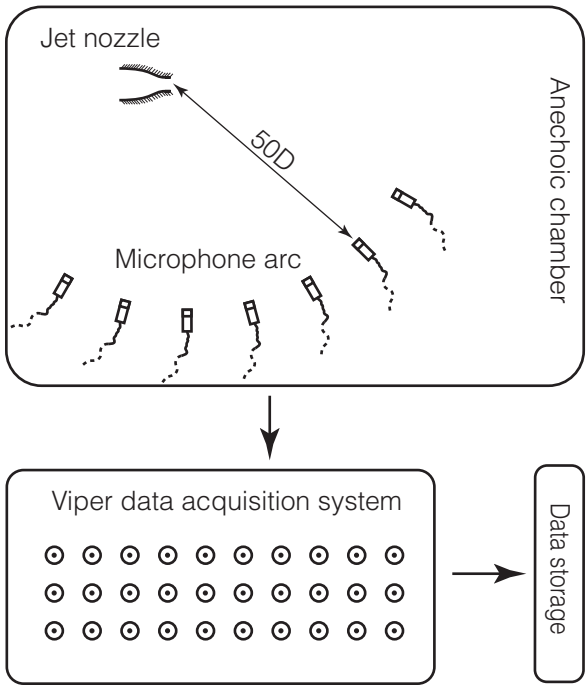

FIG. 2: Schematic illustration of the experimental setup.

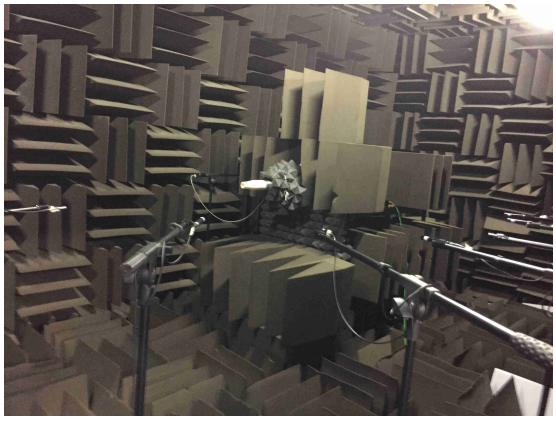

(a) The isolated jet noise experiment setup: microphones are located at 50D to the jet nozzle centre, with observer angle ranging from 30° to 120° to the jet centreline.

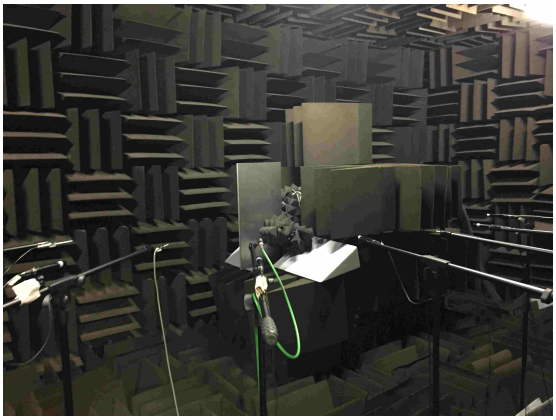

(b) The installed jet noise experiment setup: microphones are located at 50D to the jet nozzle centre on the shielded side, with observer angle ranging from 30° to 120° to the jet centreline.

FIG. 3: Experimental setup for the isolated and installed jet noise experiments.

amplified, and then digitalized at a sampling frequency of 120 kHz simultaneously using the VIPER data acquisition system from the IMC Ltd. The jet Mach number is defined by $M_0 = U_j/c_0$, where U_j is the average jet exit velocity calculated from mass flow rate using an orifice plate device, and c_0, as defined in section II, is the ambient speed of sound. To

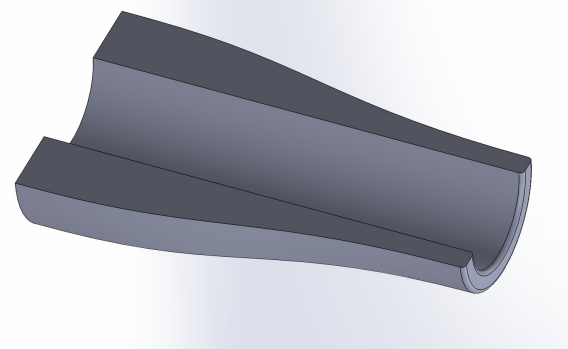

FIG. 4: The reference round nozzle used in the experiment with a diameter of 2.54 cm.

facilitate fast and flexible manufacturing, the round nozzle is 3D printed with a resolution of 0.1 mm. It is because of this that the nozzle lip, as can be seen from figure 4, has an uncharacteristically large wall thickness. Data for isolated jet noise is recorded first as reference.

To study the installation effects, a flat plate of $12D \times 24D$ is subsequently placed nearby the jet, as shown in figure 3b. The trailing edge of the plate is at L downstream from the jet nozzle, and the separation distance between the jet and the plate is H, as defined in figure 1. To obtain a comprehensive database on jet installation effects, both H and L will be varied systematically. The test matrix is shown in table I. As already mentioned, these tests are designed not only to study the effects of varying H and L on installed jet noise, but also to provide a further validation of the hybrid model[23] for a comprehensive array of plate positions.

Test No./Configuration	Mach number	H	L
1	0.5	$3D$	$6D$
2	0.5	$2D$	$6D$
3	0.5	$1.5D$	$6D$
4	0.5	$2D$	$4D$
5	0.5	$1.5D$	$4D$
6	0.5	$1.25D$	$4D$

TABLE I: Test parameters for studying the effects of varying H and L using a 2.54 cm round nozzle.

To study the effects of Mach number on installed jet noise, the jet is subsequently operated at a higher Mach number at $M_0 = 0.7$. Similar to the tests at Mach number 0.5, the plate positions are varied systematically. The complete test matrix is shown in table II. One can see that the only difference from that shown in table I is the Mach number. This is designed

Test No./Configuration	Mach number	H	L
7	0.7	$3D$	$6D$
8	0.7	$2D$	$6D$
9	0.7	$1.5D$	$6D$
10	0.7	$2D$	$4D$
11	0.7	$1.5D$	$4D$
12	0.7	$1.25D$	$4D$

TABLE II: Test parameters for studying the effects of varying Mach numbers on jet installation effects using a 2.54 cm round nozzle.

such that the Mach number effects can be studied at each of the many plate positions.

IV. COMPARISON TO OTHER EXPERIMENTAL DATA

Before discussing experimental results, it is worth comparing the current experimental data with others' published in the open literature to make sure the experimental rig is set up properly. It is sufficient to only compare the reference isolated jet noise spectra. We choose to compare with the data obtained by Tanna[26] for a cold $M_0 = 0.5$ jet. The nozzle used in Tanna's experiment had a diameter of 5.08 cm, therefore implying a Reynolds number twice as large as that in this experiment. However, since both Reynolds number are in the order of $10^5 \sim 10^6$, one can expect the difference of jet noise spectra caused by different Reynolds numbers between the two experiments to be insignificant. Comparison of the noise

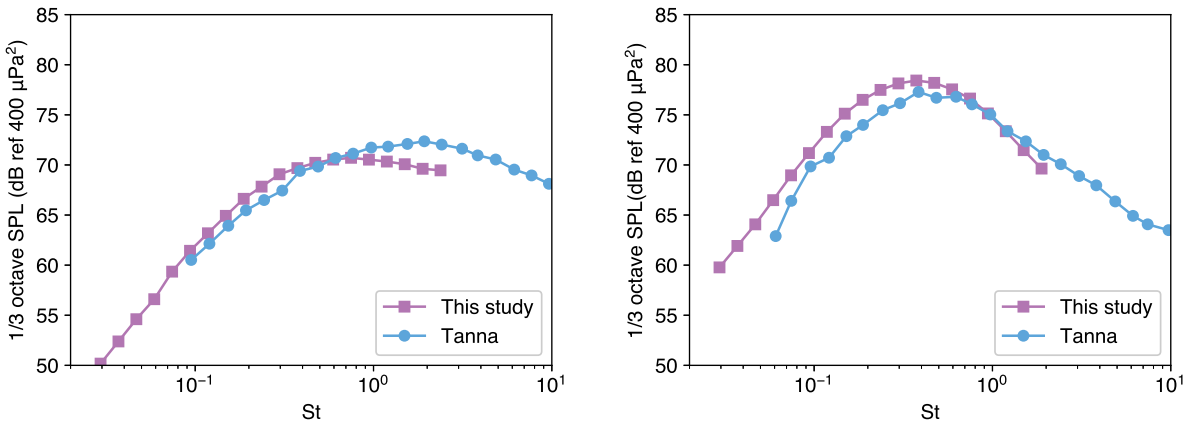

(a) $\theta = 90°$ (b) $\theta = 30°$

FIG. 5: Comparison of isolated jet noise spectra in 1/3 octaves with Tanna's. The microphones are placed at $50D$ from the centre of nozzle exit.

spectra at 90° and 30° to the jet axis are shown in figures 5a and 5b, respectively. In both figures, the Strouhal number is defined as $St = fD/U_j$. As can be seen, the far-field sound spectra at 90° agree with each other well in their spectral shapes and absolute magnitudes. There is, however, a small deviation at high frequencies. This might be due to the different nozzle shapes and inlet flow conditions. The comparison for the spectra at 30° to the jet axis shows a slightly better agreement, in particular at high frequencies. Considering the many inevitable differences between the two experiments, such an agreement is sufficient to show that the experiment is set up properly and the measurement is reliable.

V. JET NOISE SPECTRA

In this section, we present the jet noise spectra at different observer angles when the flat plate is placed at different locations. To facilitate a direct comparison, both isolated and installed jet noise spectra for various plate positions (table I) are shown in the same figures.

A. Mach 0.5 jet

We present the results for $M_0 = 0.5$ first. Far-field noise spectra on the shielded and reflected sides are shown in figures 6 and 7, respectively. Figure 6(a-c) shows the far-field noise power spectra on the shielded side when the plate's edge is at $6D$ downstream from the jet nozzle but at different radial positions. Both isolated and installed jet noise spectra are shown. In figure 6(a), one can clearly see that the plate enhances the lower-frequency jet noise by up to 10 dB. This noise enhancement is most pronounced at an angle close to 90° to the jet centre line. The noise enhancement at 30°, however, is virtually negligible. This is consistent with the earlier findings[2,8,9,13,18,27,28] and the edge-scattering mechanism proposed in the earlier paper[23] (at low frequencies, the scattered sound has a dipolar, rather than a cardioid directivity pattern). In the intermediate- and high-frequency range, jet noise is effectively shielded by the flat plate at angles close to 90° to the jet axis, while these shielding effects diminish at lower observer angles. Figure 6(b) shows the spectra when the plate is at a closer distance to the jet at $H = 2D$. It can be seen that the noise enhancement at low frequencies is now more pronounced, increasing to more than 15 dB. Also, it can be observed that the noise increase also occurs in the intermediate frequency range at high observer angles. An observable noise increase occurs at 30° to the jet axis as well. In the high-frequency regime, one can see that the plate still serves as an effective noise shield at high observer angles, but little has changed for the shielding effects compared to figure 6(a). Moving the plate closer to $H = 1.5D$, as shown in figure 6(c), results in an even stronger noise enhancement. The peak noise increase is now up to 20 dB at 90°. At such a close proximity to the plate, jet noise at 90° is larger than that at 30°. The frequency range of

noise increase becomes even wider, leading to louder noise in the intermediate range. In figure 6(a-c), it is shown that the enhanced noise spectra at low frequencies exhibit a clear oscillation pattern. This oscillation is more marked when the plate is closer to the jet. A detailed discussion on this is provided in Appendix A.

The widening of the enhanced frequency range is thought to be closely related to the radial decay rates of the instability waves. As describe in section II, when the ambient flow is static, the decay rate of the instability wave has a dominant exponential form similar to $\exp(-\gamma_c r)$,[29] where

$$\gamma_c = \sqrt{k_1^2 - k^2}. \tag{10}$$

Therefore, as the frequency increases, γ_c increases. This implies that high-frequency instability waves decay more quickly as the radial coordinate increases. Consequently, if we place the plate sufficiently far-away from the jet, only low-frequency instability waves can be seen and scattered into sound by the flat plate. On the other hand, if the plate is moved closer to the jet, high-frequency instability waves become stronger, leading to an enhanced scattering noise at higher frequencies.

The measured noise spectra when the plate is at $L = 4D$ are shown in figure 6(d-f). The observer is still on the shielded side of the plate. Figure 6(d) presents the results when $H = 2D$. At such a distance, the noise amplification is around 8 dB with an observable increase up to 2 kHz ($St \approx 0.3$). Noise increase is, as expected, occurring only at high observer angles. At high frequencies, the noise is reduced by around 3 dB by the shielding effects. Moving the plate closer to the jet clearly causes a stronger noise increase, as shown in figure 6(e), where $H = 1.5D$. At such a distance, the maximum noise amplification observed is around 12 dB at 90° to the jet centre line. However, there is little noise increase at 30°. When the plate is placed at $H = 1.25D$, the tendency of stronger noise enhancement at a closer distance between the plate and the jet continues. A noise increase up to 16 dB is observed. The affected frequency range continues to be wider. The shielding effects remain roughly the same.

The effects of varying H on the installed spectra on the shielded side are clearly demonstrated by comparing figures 6(a) to 6(c), and figures 6(d) to 6(f). The effects of varying L at fixed H can be revealed by comparing figures 6(b) and 6(d), and figures 6(c) and 6(e). When the plate is placed at $H = 2D$, the noise amplification at $L = 6D$ is clearly much more pronounced than that at $L = 4D$, with the former one being up to 15 dB and the latter one being up to 8 dB. The affected frequency range remains roughly the same. However, it can be seen that the shielding effects are much more effective when the plate is located further downstream. Another difference is the observable noise enhancement at $L = 6D$ but negligible noise increase at $L = 4D$ at 30° to the jet centre line. When the plate is placed at $H = 1.5D$, the same tendency remains, while both configurations result in louder noise because of a closer distance to the jet.

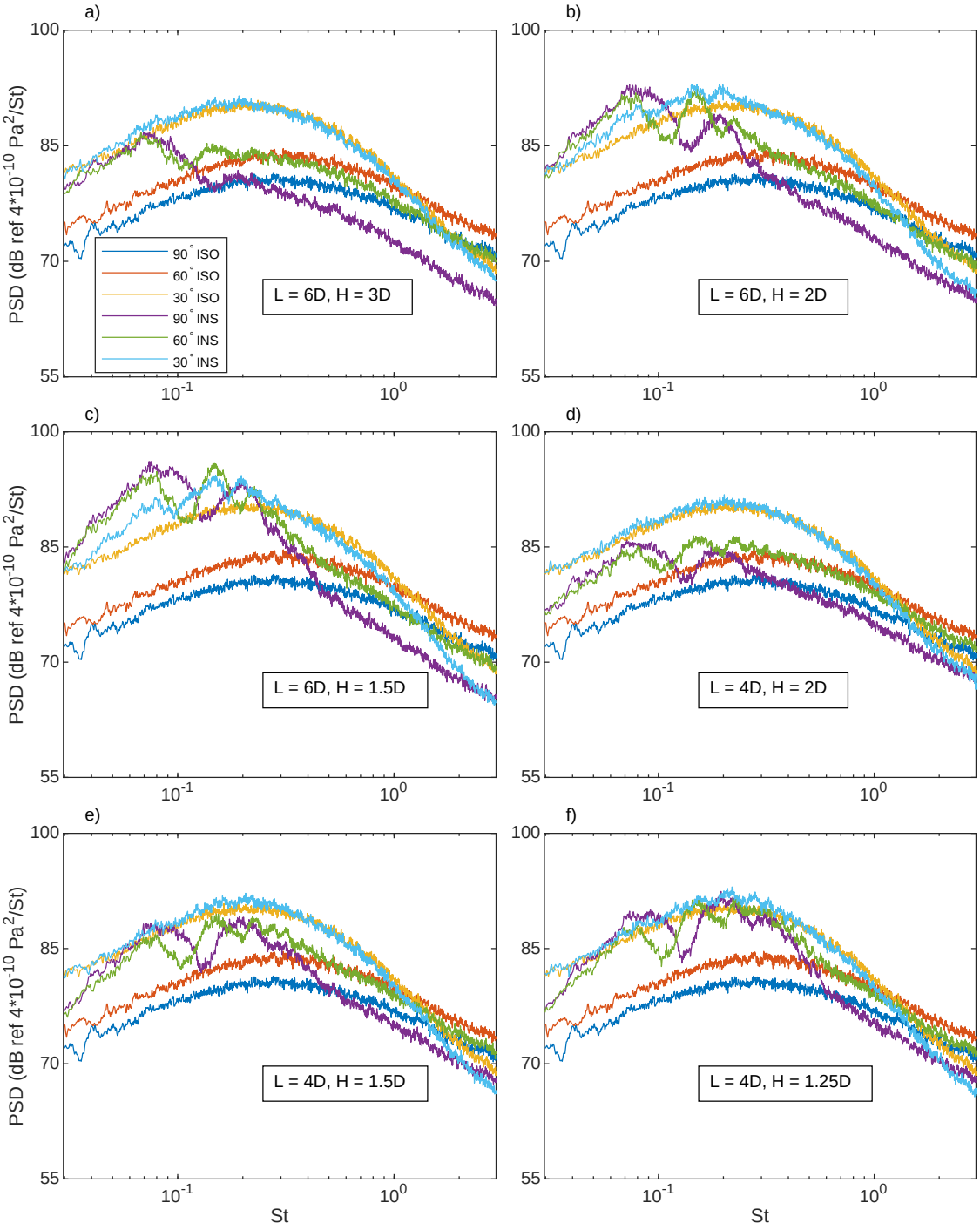

FIG. 6: Isolated and installed noise spectra of a Mach number 0.5 jet at 90°, 60° and 30° to the jet centreline on the shielded side, for various plate positions shown inside each figure.

Experimental results measured on the other side of the plate, i.e. the reflected side, are presented in figure 7. Figure 7(a-f) shows the noise spectra when the plate is at the same positions as those shown in figure 6(a-f). At low frequencies, a significant noise increase is observed, resembling the behaviour on the shielded side, see figures 7(a) to 7(f). Moreover,

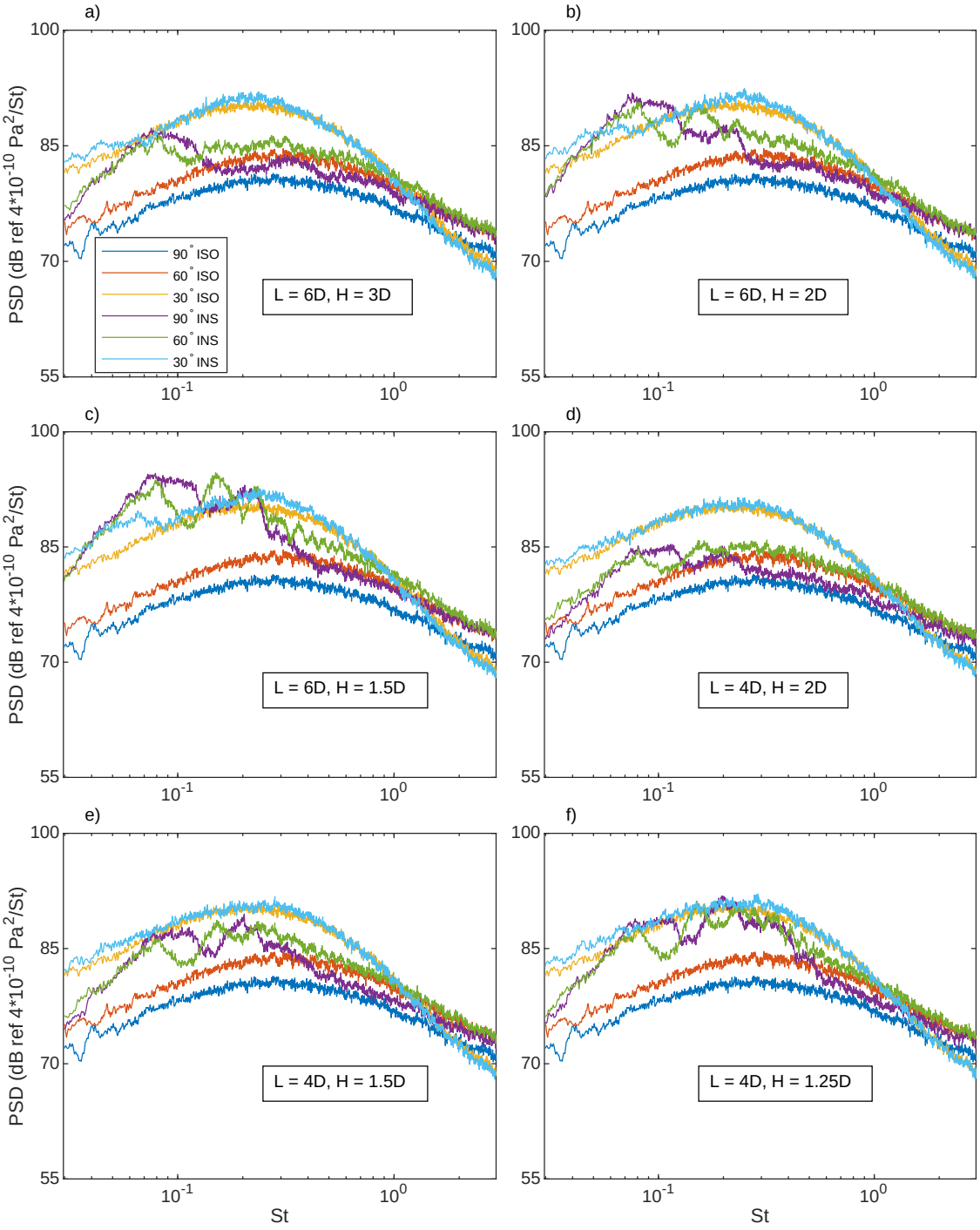

FIG. 7: Isolated and installed noise spectra of a Mach number 0.5 jet at 90°, 60° and 30° to the jet centreline on the reflected side, for various plate positions shown inside each figure.

comparing figures 7(a) to 7(c) (and figures 7(d) to 7(f)) reveals the same behaviour of louder noise for smaller H, when L is fixed. The enhanced sound spectra appear to be nearly identical to those shown in figure 6. However, a careful examination shows they are not. The most important difference occurs around the lowest frequencies. For example,

comparing figures 6(a) and 7(a) indicates that the noise increase is somewhat less pronounced at 90° and 60°. On first thought, this would invalidate the proposed near-field scattering mechanism, which entails a perfectly symmetric noise radiation across the plate. However,

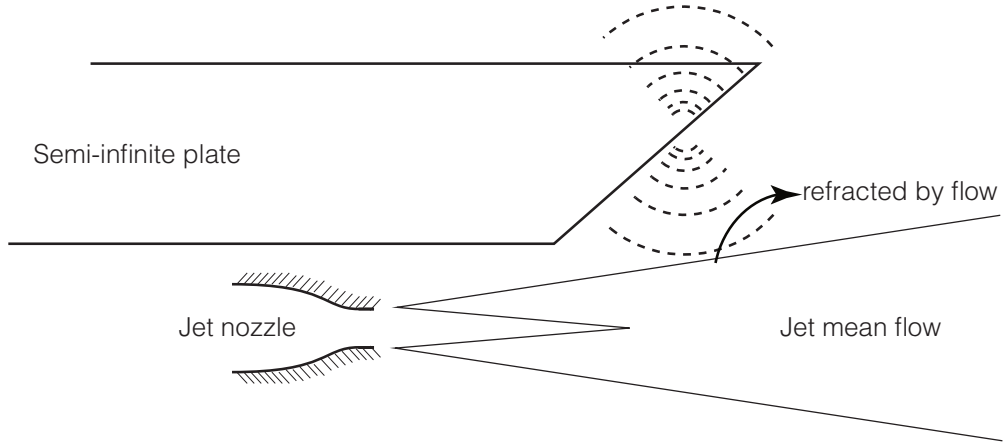

FIG. 8: The schematic diagram illustrating the refraction effects of the jet mean flow on the reflected side of the flat plate.

revisiting the full problem suggests that this is caused by the refraction effects of the jet mean flow on the reflected side. To show this more clearly, a schematic diagram is presented in figure 8. As can be seen, the scattered sound originates near the edge and propagates both above and below the edge. However, the sound has to pass through the jet plume in order to reach an observer placed in the far-field on the reflected side. This is different on the other side, where no jet plume is present. Therefore, the discrepancies between the observed spectra on both sides are due to the jet refraction effects. Decreasing the value of L, as can be seen by comparing figures 7(b) and 7(d) (or figures 7(c) and 7(e)), causes the noise increase to be less significant.

However, the installation effects in the high-frequency regime are considerably different from those on the shielded side. As suggested by its name, noise increase is observed for spectra on the reflected side due to sound reflection at high frequencies by the plate. Figure 7(a) shows that the high-frequency noise increase is most pronounced at 90°, and less so at small observer angles (small θ). Comparing figures 7(a) to 7(c) (and figures 7(d) to 7(e)), one can see that changing H while L is fixed does not significantly change this reflection-caused noise increase at all observer angles, in contrast to the low-frequency noise enhancement. On the other hand, shortening L causes high-frequency reflection to be less notable. For example, one can find, by comparing figures 7(b) and 7(d), that noise increase at high frequencies is up to 3 dB when $L = 6D$ while only half is achieved when $L = 4D$ (at 90°).

In summary, installed jets exhibit a significant noise increase at low frequencies compared to isolated jets. The noise spectra have slightly non-symmetric dipolar directivity patterns

due to the asymmetry caused by jet refraction. At high frequencies, jet noise is noticeably suppressed due to the plate shielding effects on the shielded side and slightly (e.g., around $2-3$ dB) enhanced on the reflected side. Decreasing H while L is fixed results in a stronger noise increase at low frequencies. At high frequencies, on the other hand, it causes little change to both the shielding and reflecting effects. Decreasing L while H is kept constant results in less significant noise increase at low frequencies. In addition, at high frequencies, both the shielding and reflecting effects become noticeably less effective.

B. Mach 0.7 jet

Experimentally measured installed jet noise spectra for $M_0 = 0.7$ are presented in figures 9 and 10. Since jet noise power scales as the eighth power of jet Mach number,[30] one can see that considerably larger noise spectra are observed compared to those shown in figure 6 and 7. Nevertheless, figure 9 is qualitatively similar to figure 10 in nearly all aspects. For example, significant noise increase for installed jets occurs only at low frequencies, placing the plate closer to the jet (decreasing the value of H while L is fixed) results in a stronger noise increase at low frequencies, decreasing L while H is kept constant results in less significant noise increase at low frequencies, etc. A more detailed discussion of these characteristics is given at the end of the preceding section.

It is interesting to note the differences between the spectra at $M_0 = 0.5$ and $M_0 = 0.7$. One of the most striking differences is that the low-frequency noise enhancement is less significant for the $M_0 = 0.7$ jets when the plate is placed at the same positions. For instance, the maximum noise increase shown in figure 6(c) is around 20 dB while in figure 9(c) around 15 dB. The same conclusions can be reached by comparing other pairs of spectra. This is believed to be due to the dependence of the installed jet noise on jet Mach number. We have mentioned in section I that the intensity of installed jet noise scales as the sixth power of the jet Mach number, while the isolated jet noise intensity scales as the eighth power. Therefore, when the Mach number increases, isolated jet noise power increases more quickly, hence narrowing the relative difference between the installed and isolated noise spectra. This trend is more evident by contrasting figures 6(f) and 9(f).

The experimental results obtained in this section are consistent with earlier findings. In addition, attention has also been paid to the effects of varying H, L and M_0 on the high-frequency installation behavior and the non-symmetric dipolar directivity due to the refraction effects of the jet plume. Full spectra at different observer angles for different H, L and M_0 combinations are presented in a detailed narrow-band manner. Such a comprehensive database would be valuable in future studies.

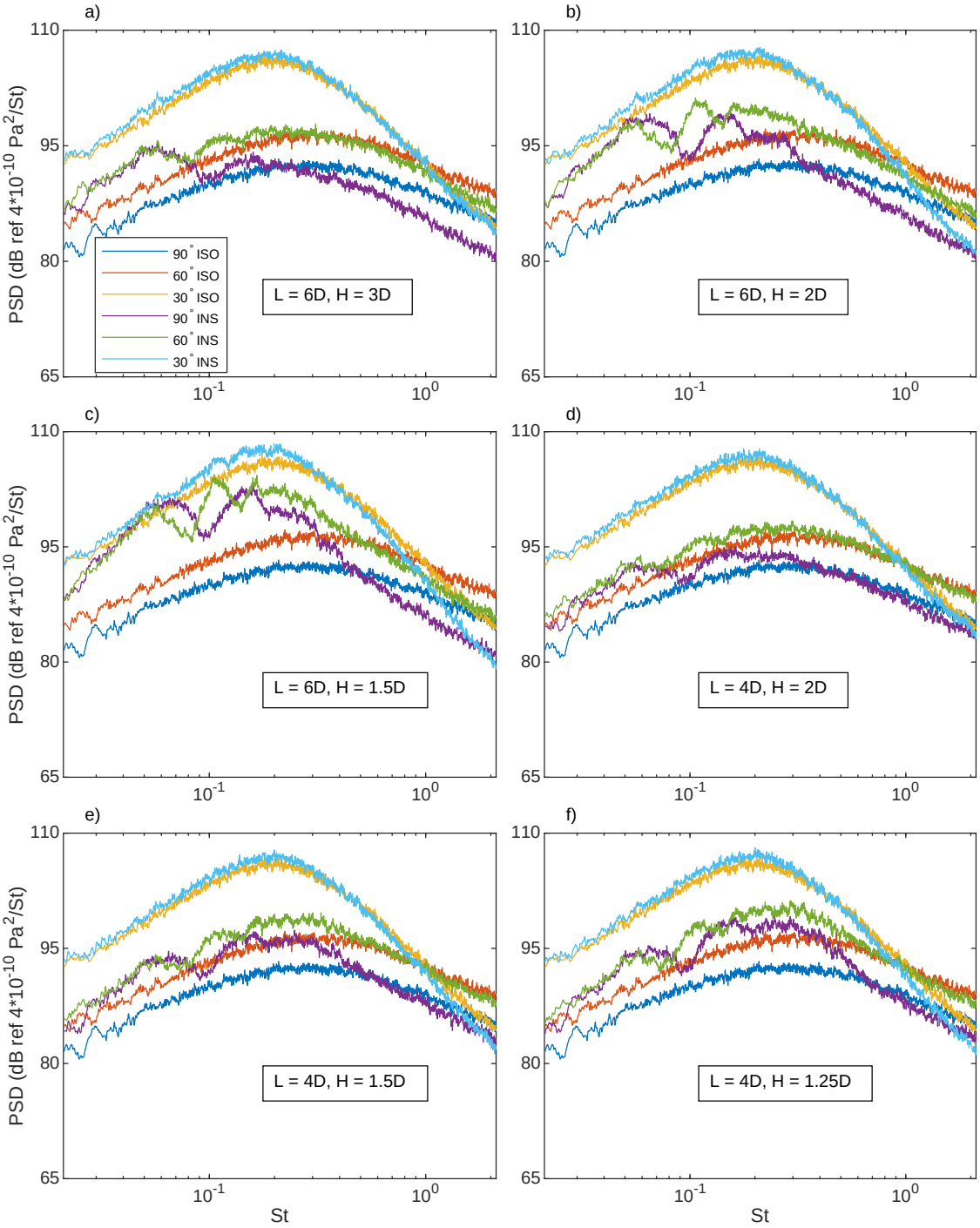

FIG. 9: Isolated and installed noise spectra of a Mach number 0.7 jet at 90°, 60° and 30° to the jet centreline on the shielded side, for various plate positions shown inside each figure.

VI. COMPARISON WITH THE PREDICTION MODEL

With a comprehensive set of experimental data on installed jet noise for different plate positions available, we can compare them to the predictions of the hybrid model briefly

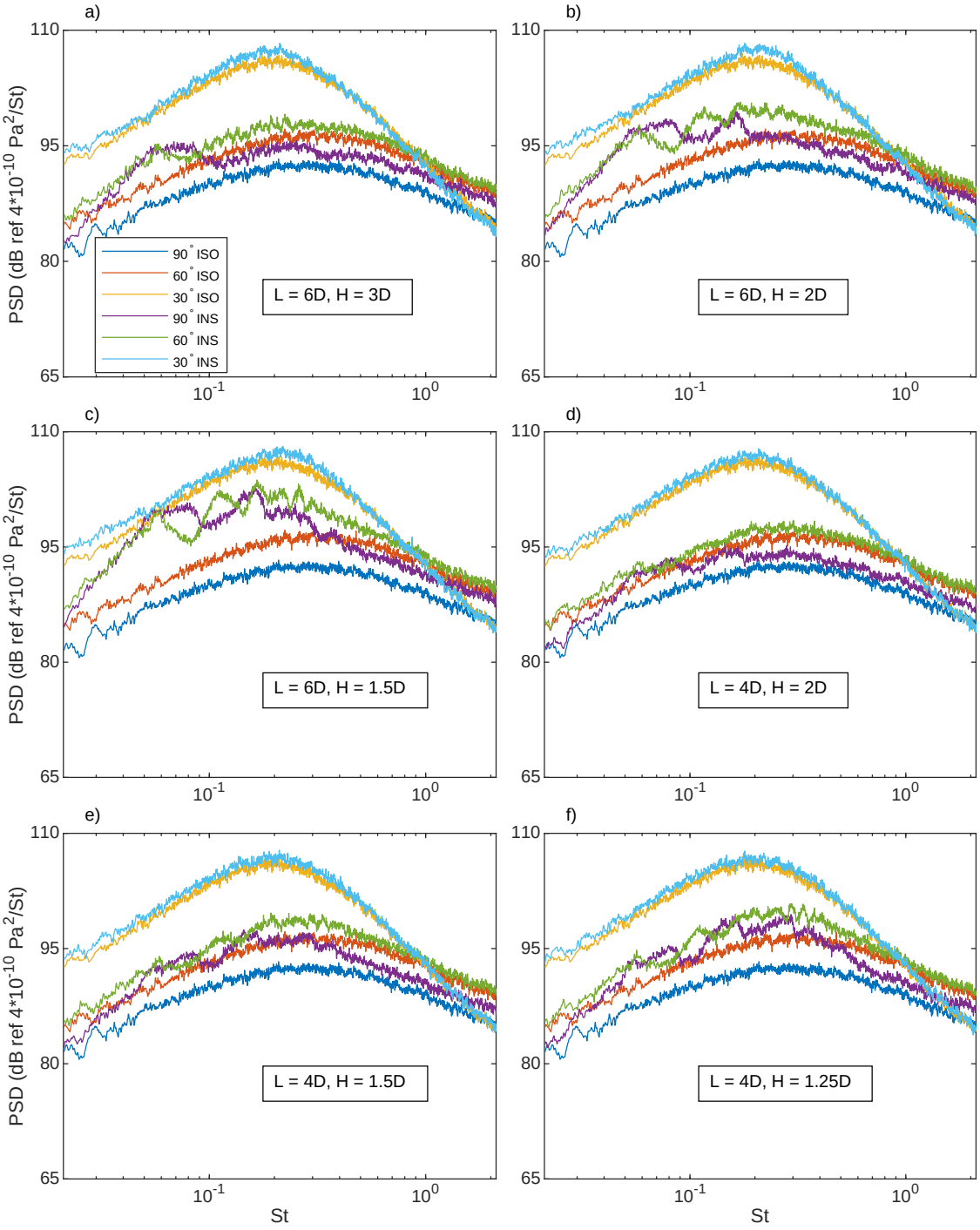

FIG. 10: Isolated and installed noise spectra of a Mach number 0.7 jet at 90°, 60° and 30° to the jet centreline on the reflected side, for various plate positions shown inside each figure.

described in section II. In particular, the innovative instability-wave-scattering model can be properly validated. We chose to compare the spectra at $M_0 = 0.5$. To do so, the PSD of the near-field pressure fluctuations must be measured and used as an input to the model.

For convenience we also use the cylindrical coordinates centred around the jet exit with z in the streamwise, r in the radial and φ in the azimuthal directions respectively.

A. The near-field pressure

Figure 11(a) shows the power spectral densities of the near-field pressure at $z = 6D$ but at various radial positions. It should be noted that these spectra are obtained using

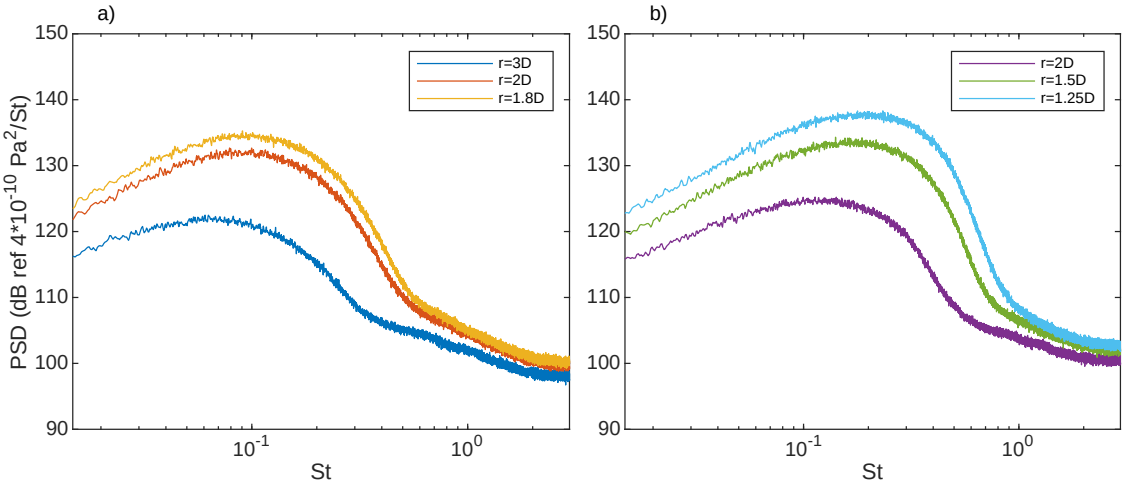

FIG. 11: The power spectral densities of the near-field pressure at various radial positions but at two fixed streamwise locations: a) $z = 6D$; b) $z = 4D$.

one near-field microphone (not to be confused with the far-field microphones) placed at a specific azimuthal angle (not using a near-field azimuthal microphone arc). Therefore, they are different from the modal pressure spectra mentioned in section II. However, as noted in the earlier paper,[23] when the frequencies of interest are low, the sound due to near-field scattering can be calculated by using the PSD of the near-field pressure at a specific point. From figure 11(a), it can be seen that the near-field pressure fluctuation decays quickly as the radial coordinate r increases in the low and intermediate frequency regime. For example, a decrease of up to 15 dB is observed from $r = 2D$ to $3D$. However, in the high-frequency regime, little change occurs. This is because the spectra in the low-to-intermediate frequency range are dominated by the signature of the instability waves, while acoustic perturbations dominate the near-field pressure fluctuations at high frequencies, as demonstrated in the earlier paper.[23] Also it can be observed that the spectral decay (due to moving the microphone away from the jet) gradually increases as the frequency increases, compatible with the behaviour of the modified Bessel functions of the second kind (see Lyu, Dowling, and Naqavi[23] for details).

Figure 11(b) shows the spectra at $z = 4D$. Comparing with figure 11(a), two distinctions can be readily observed. Firstly, the spectra at $z = 4D$ but at the same radial position have

smaller amplitudes, especially at low frequencies. This is consistent with the convecting growing behaviour of jet instability waves.[31,32] It is also consistent with the observation that the installed jet noise is louder when the plate is placed further downstream (but at the same radial positions, see the discussion on this in section V). Secondly, spectra at $z = 4D$ have higher peak frequencies. This is expected since it is known that instability waves at high frequencies saturate earlier.[31,33]

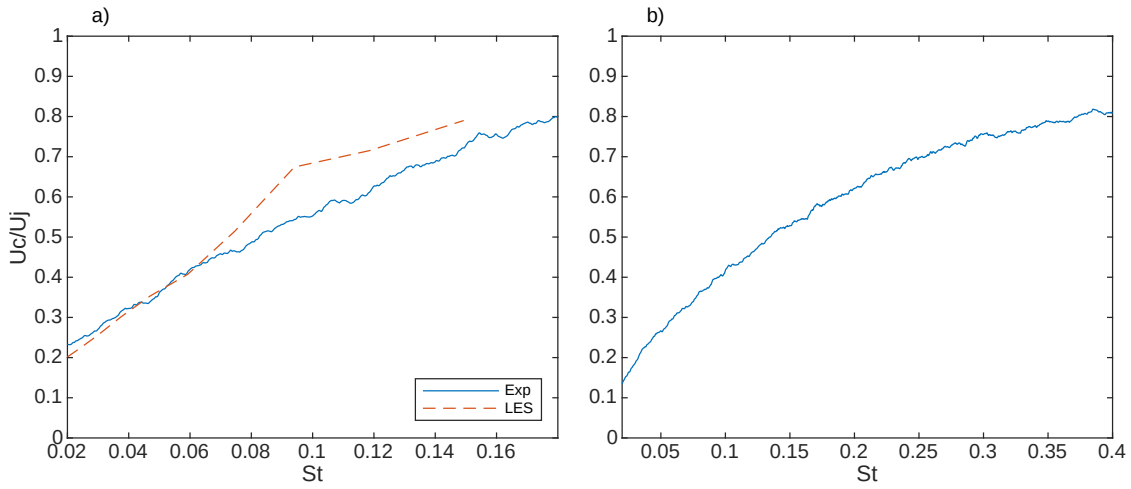

FIG. 12: The convection velocities obtained from examining the radial decay rates of the near-field pressure PSDs at two different streamwise locations: a) $z = 6D$; b) $z = 4D$.

The hybrid model described in section II requires the spectral strengths and the frequency-dependent convection velocity of the near-field instability waves as inputs. In the earlier paper,[23] this is calculated from analysing an LES database. A similar analysis can be performed with the experimental data if we measure the near-field pressure using a microphone arc, such as the one used by Tinney and Jordan.[34] But for simplicity, instead of using the modal spectra, we use the overall spectra measured at one point. As discussed in the earlier work,[23] this is permissible, since the decay rates of the zero- and first- order instability waves do not differ from each other significantly, in particular at low frequencies. The convection velocity can also be estimated by making use of this fact, i.e., we assume the point spectra decay at the same rate as the zeroth-order instability waves. The convection velocities obtained by examining the decay rates of the spectra shown in figure 11 are plotted in figure 12. Only low-frequency results are shown because of the dominance of acoustic fluctuations at high frequencies. The result for $z = 6D$ is shown and compared with that obtained from LES in figure 12(a). Very good agreement is achieved. This not only shows that the convection velocity is indeed frequency-dependent, but also provides another piece of evidence for having an accurate LES database. Figure 12(b) presents the convection velocity for the instability waves at around $z = 4D$. Though the two curves in figures 12(a) and 12(b) look qualitatively similar to each other, they are not strictly identical. This is expected, since

the mean flows at different streamwise locations are different, so are the characteristics of jet instability waves.

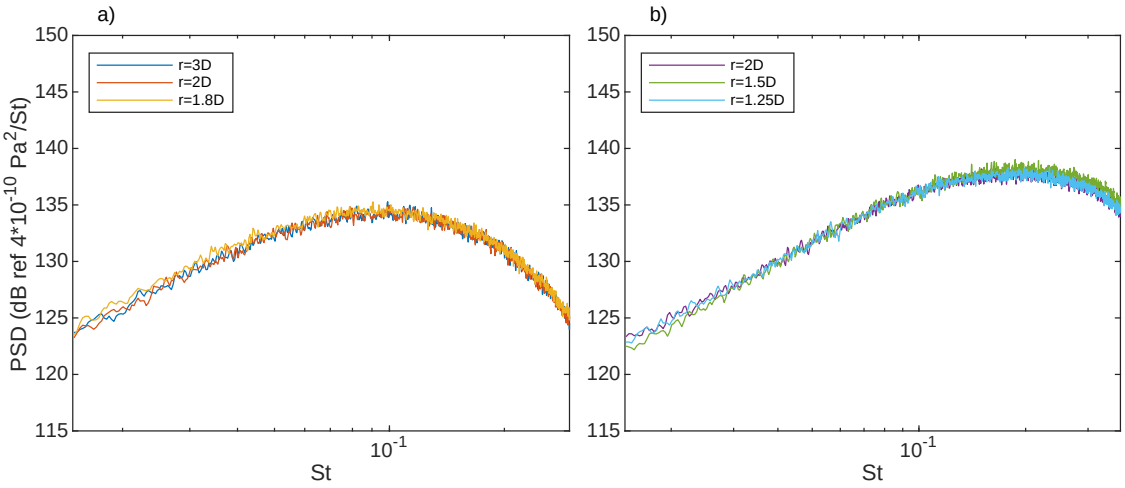

FIG. 13: The collapsed power spectral densities of the near-field pressure using obtained convection velocities at various streamwise locations: a) $z = 6D$; b) $z = 4D$.

Using the convection velocities obtained in figure 12, the PSDs at various radial locations (but the same streamwise location) can be successfully collapsed, as can be seen from figure 13. The plotted quantity in figure 13 is the scaled PSD defined by[23]

$$\frac{\Pi_0(\omega; r_0)}{K_0^2(\gamma_c r_0)}, \tag{11}$$

where $\Pi_0(\omega; r_0)$ denotes the overall PSD of the near field pressure fluctuation measured at $r = r_0$. Note that the shown frequency range is corresponding to the frequency range shown in figure 12. Excellent agreement is achieved for spectra at both $z = 6D$ and $z = 4D$, though there is slight disagreement near the highest frequency for the spectra $z = 4D$. This is somewhat expected since we assume different modal instability waves to decay at the same rate (at the rate determined by the zeroth-order modified Bessel function of the second kind). But high-order instability waves are more likely to exist at upstream locations.[35]

B. Validation of the hybrid prediction model

Equipped with the flow data from similar RANS simulations to that described in the earlier paper,[23] the frequency-dependent convection velocity and the near-field pressure PSDs from experiment, the hybrid model can be evaluated readily. The near-field pressure PSD measured at the smallest value of r_0 is used as the input for each value of L. Using those measured at other values leads to negligible change to the far-field predictions. This is because the instability waves decay with radial distance is accurately predicted with the use

of the frequency-dependent convection velocity. The predicted sound spectra are compared with experimentally measured PSDs at various observer angles and for various plate positions. In the rest of this section, comparisons are shown for six observer angles for each plate position, i.e., 90°, 60° and 30° to the jet axis on both the shielded and reflected sides of the flat plate.

1. For plate position at $L = 6D$

Figure 14 shows the comparison of the isolated and installed jet noise spectra when the plate's trailing edge is at $L = 6D$ and $H = 3D$. We should emphasise here that the isolated jet noise spectra are predicted using the Lighthill's acoustic analogy described in section II with a free-field Green's function, and so neglect the refraction effects by the mean flow. We discuss the results on the shielded side first (figure 14(a-c)). The agreement between the isolated spectra at $\theta = 90°$ (figure 14(a)) is very good, apart from a slight over-prediction at high frequencies. The installed spectra are much more interesting. At such a distance to the jet, the maximum noise enhancement at low frequencies caused by the scattering of instability waves is around 10 dB. This is well captured by the model. At high frequencies, noise is effectively shielded by the plate. This is qualitatively captured by the prediction model (though the predicted amplitude is not very different from the experimental results as well). This discrepancy may be explained by the fact that jet refraction effects are not included in the Lighthill acoustic analogy part of the hybrid model.[23] Figure 14(b) shows the comparison for $\theta = 60°$. The prediction for the isolated spectrum starts to deviate from the experimental result at high frequencies due to the neglect of jet refraction effects, though at low frequencies the agreement is still acceptable. For the installed noise spectra, as discussed in the preceding section, weaker noise enhancement and shielding effects are observed experimentally. The model can successfully capture this and agrees with the experimental results at low frequencies. The trend of weaker shielding effects is also exhibited by the model. The spectra comparison at $\theta = 30°$ is more interesting. One can see that at such a low observer angle, jet refraction is significant, even for low frequencies. Therefore, the deviation between the experiment and the prediction for isolated noise spectra can be as large as 5 dB. However, the fact that there is little noise enhancement at low frequencies and little noise suppression at high frequencies is captured remarkably well. In other words, the model successfully captures the physics of jet installation, although the absolute values of the predicted spectra are affected by the refraction effects. This indicates that apart from refraction effects, the agreement for installed jet noise spectra is very good.

Noise comparison on the reflected side is shown in figure 14(d-f). Since the isolated jet noise spectra are identical to those on the other side of the plate, we only need to focus on the installed spectra. Figure 14(d) shows the results at 90° to the jet axis. Excellent

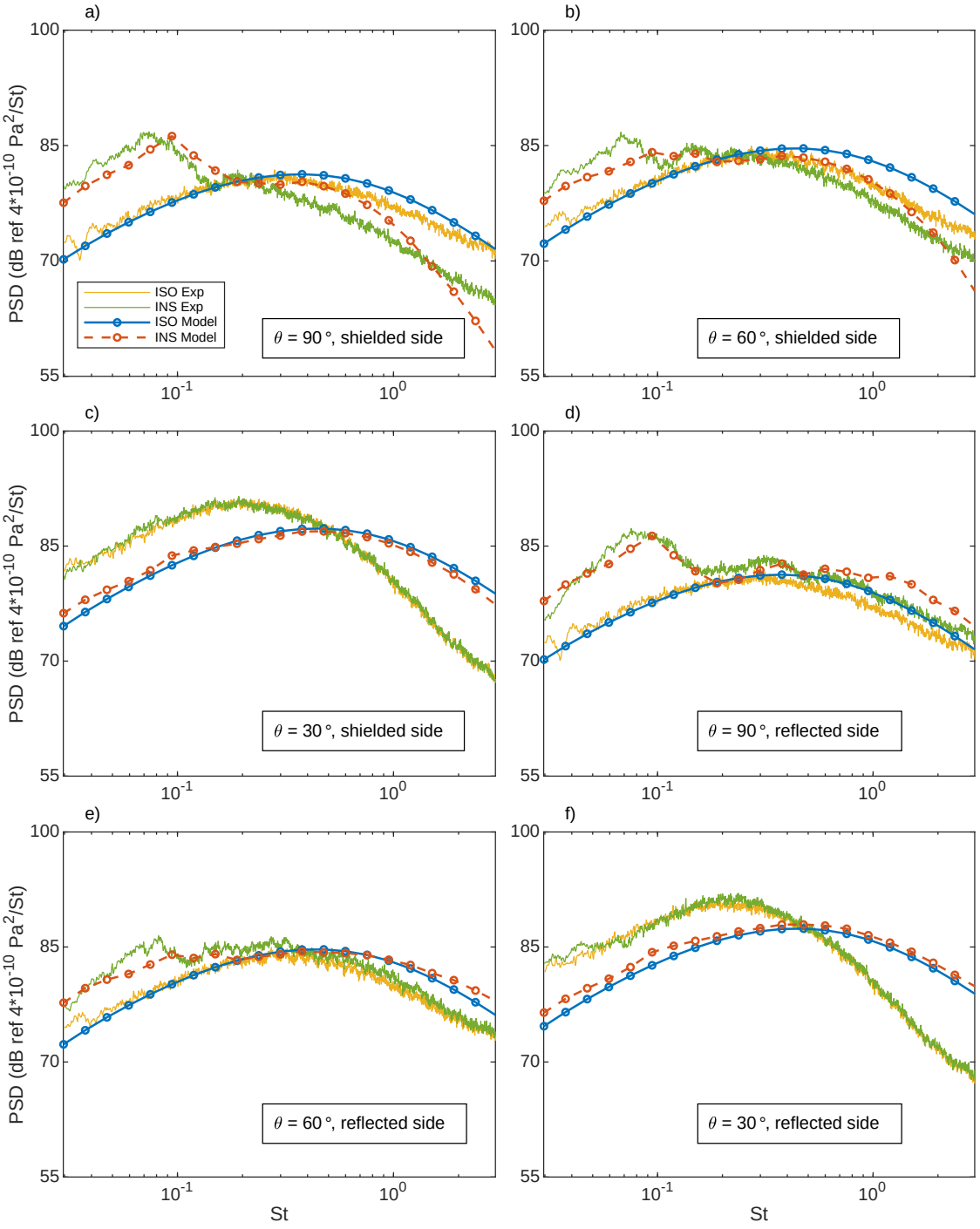

FIG. 14: Comparison of the predicted isolated and installed noise spectra with experimental results at various observer locations for $L = 6D$ and $H = 3D$.

agreement at this observer angle is achieved since there are no (little) refraction effects. At low frequencies, the prediction is identical (symmetric) to that on the other side of the plate and the agreement continues to be good. At high frequencies, the noise increase of around 3 dB is successfully predicted by the model. The slight over-prediction for the

high-frequency installed spectrum is apparently caused by the slight over-prediction of the isolated spectrum. Comparison of noise spectra at 60° to jet axis is shown in figure 14(e). As discussed above, the same level of agreement as on the other side of plate is achieved at low frequencies. However, we see that the predicted spectrum gradually deviates from the experimental spectrum at high frequencies due to the refraction effects. The tendency of weaker noise increase due to reflection at lower observer angles is captured. Figure 14(f) shows the comparison at 30° to the jet axis. This is very similar to the results on the other side of the plate, for the same reasons.

Comparison of the spectra when the plate's trailing edge is at $L = 6D$ and $H = 2D$ is shown in figure 15. Again, identical isolated jet noise spectra suggest that we only need to discuss installed spectra. Figure 15(a) shows excellent agreement between the experimental and predicted spectra at $\theta = 90°$. The low-frequency noise intensification is much more pronounced at such a plate position and is predicted remarkably well. Even the high-frequency shielding effects are predicted reasonably well. Note that there are small oscillations in the experimental spectrum, which are not captured very well by the model. One can show that this oscillation is due to the finite chord length of the flat plate (see more details in Appendix A). The model makes use many approximations in order to reach a simplified formula, which might be the reason for not capturing these low-frequency oscillations. However, the predicted spectrum does follow the mean experimental counterpart very closely. Figure 15(b) shows the results for an observer at $\theta = 60°$. Excellent agreement continues to be achieved at low frequencies, while the high-frequency prediction sees discrepancies due to refraction effects. Figure 15(c) deserves a detailed explanation. At first glance it appears that the prediction yields a much higher noise enhancement at low frequencies, which does not agree with experimental observations. However, one should bear in mind that the total power spectral density Φ is the sum of Φ_Q and Φ_N. Therefore, a lower value of Φ_Q (which is exhibited by the much lower value of the isolated spectrum in the figure and the fact that the isolated spectrum is nearly identical to the installed spectrum at low frequencies) would contribute little to Φ and the total spectrum Φ is nearly solely determined by the large value of Φ_N. Hence Φ would be much larger than Φ_Q (hence the isolated spectrum, which explains the significant noise augmentation predicted in figure 15(c)). However, if Φ_Q had been correctly predicted to be of larger values, the contribution from Φ_N would have been much less pronounced, and one would have expected only a slight noise increase. Therefore, the seemingly discrepancy at low frequencies is due to the inaccurate prediction of the isolated jet noise spectrum and the near-field scattering model works remarkably well (we can see evidence of this if we add the Φ_N to the isolated spectra measured in the experiment).

The comparison on the reflected side is shown in figure 15(d-f). Excellent agreement is observed at 90° to the jet axis (see figure 15(d)). The less good agreement at the lowest frequencies is caused, as mentioned in the preceding section, by the refraction of the reflected

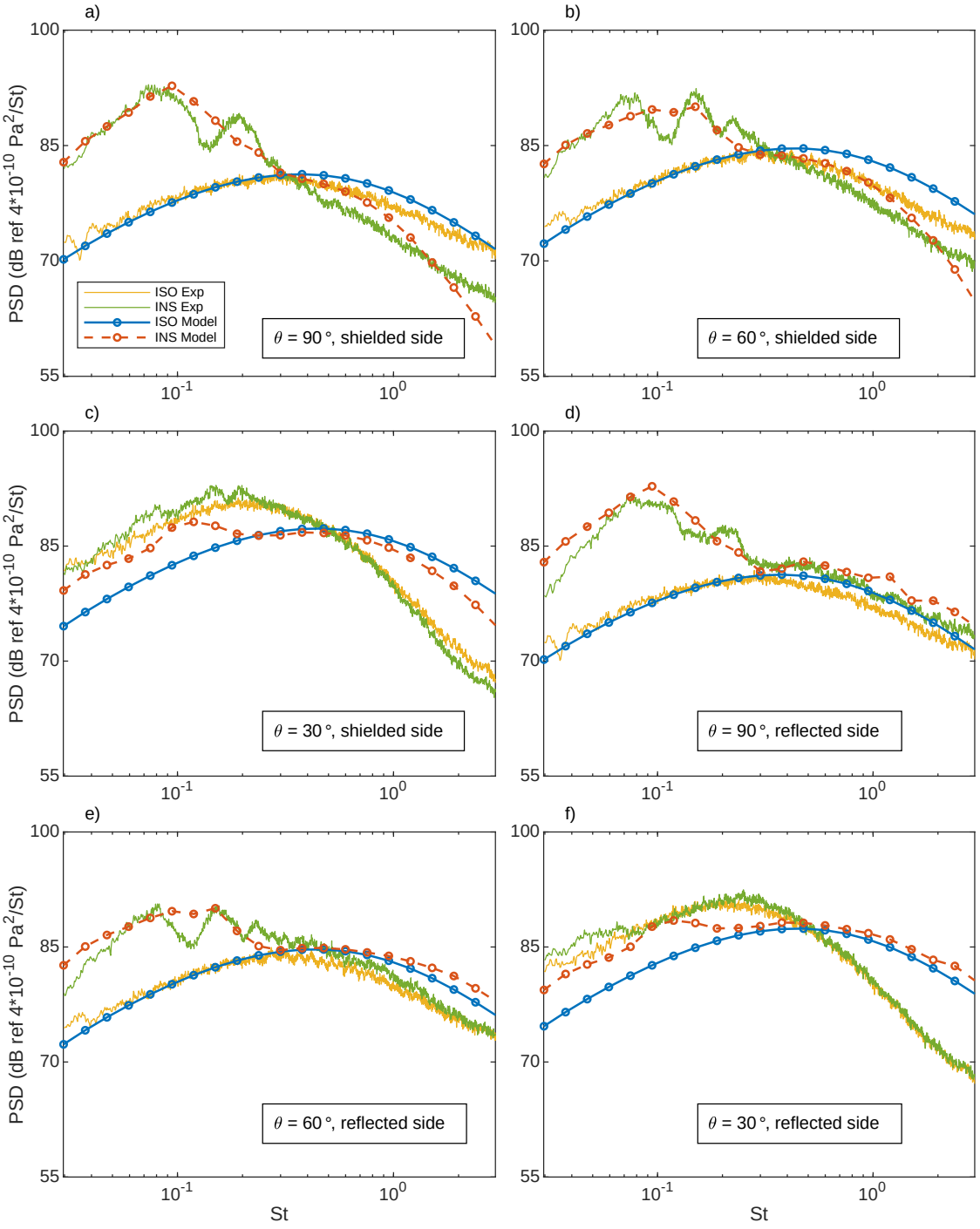

FIG. 15: Comparison of the predicted isolated and installed noise spectra with experimental results at various observer locations for $L = 6D$ and $H = 2D$.

sound by the jet, which is not accounted for in this model. High-frequency agreement is nearly identical to that shown in figure 14(d). Figure 15(e) shows the results when the observer is at 60° to the jet axis. Apart from the larger noise intensification, which is correctly captured by the model, it is again similar to the comparison shown in figure 14(e).

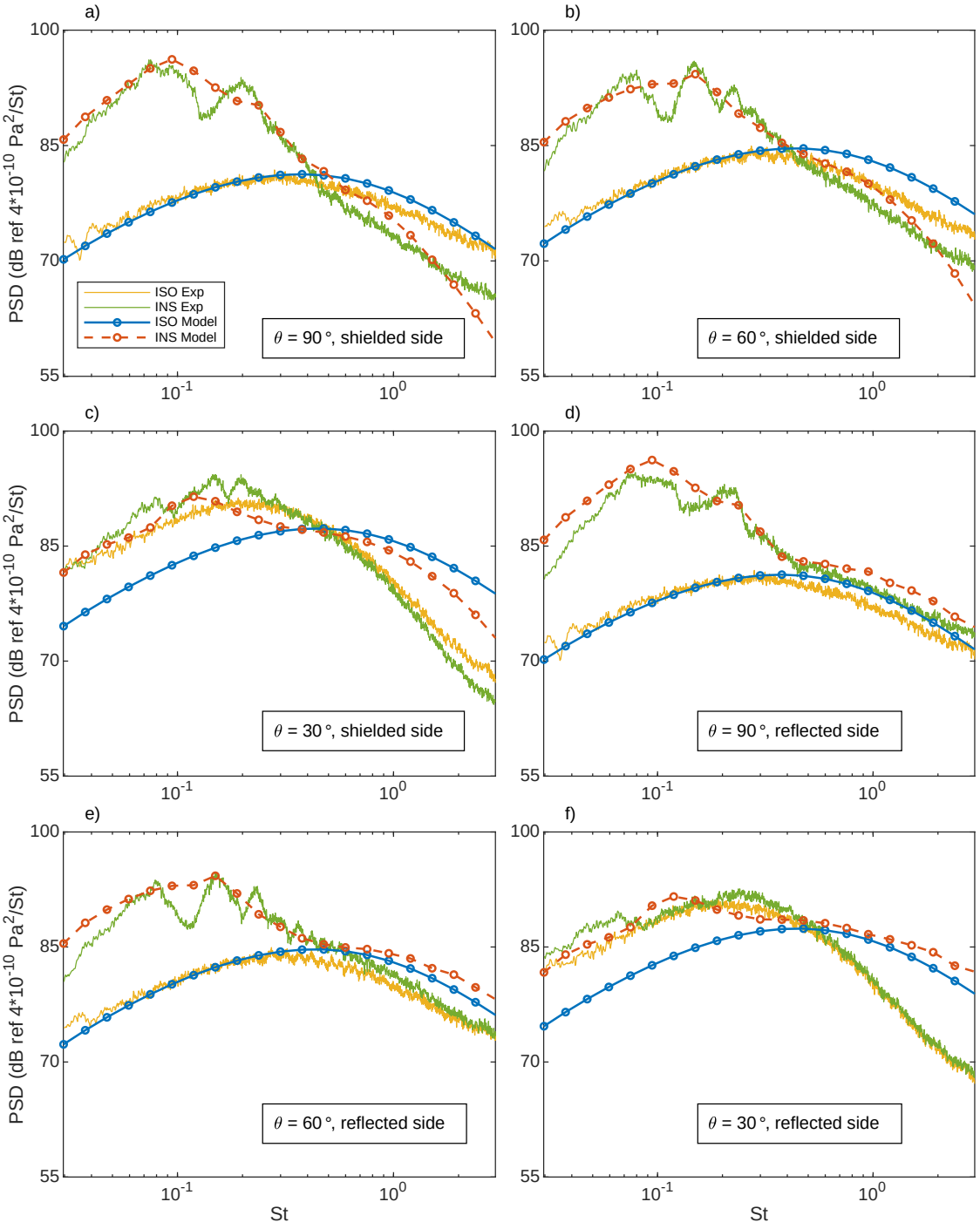

FIG. 16: Comparison of the predicted isolated and installed noise spectra with experimental results at various observer locations for $L = 6D$ and $H = 1.5D$.

So are the results shown in figure 15(f).

When the plate is moved closer to the jet at $H = 1.5D$, a significant noise increase of up to 20 dB is achieved. The comparison of the model prediction with experimental results at such a close distance is shown in figure 16. The hybrid model, especially the instability-

wave-scattering model predicts the noise enhancements at all angles remarkably well. Note again that the seemingly over-prediction of the low-frequency enhancement in figures 16(c) and 16(f) is caused by the inaccurate prediction of the isolated spectra.

2. For plate position at $L = 4D$

Comparison of the isolated and installed jet noise spectra when $L = 4D$ and $H = 2D$ is shown in figure 17. As already noted in the section discussing the experimental results, moving the plate towards jet nozzle causes the noise increase at low frequencies to be less significant. Results are again shown for both the shielded (figure 17(a-c)) and reflected sides (figure 17(d-f)). At $\theta = 90°$ on the shielded side, a noise increase of up to 8 dB is found. The prediction yields a noise increase of around 5 dB, slightly below the experimental results. It is suggested that this could be either due to the spectral oscillations or because the approximation that the instability waves of different azimuthal modes decay at roughly the same rate is less good at $z = 4D$ (because the instability waves of higher azimuthal modes do not vanish as quickly as those at $z = 6D$, see Tinney, Glauser, and Ukeiley[35] and Tinney and Jordan[34] for instance). Comparison at $\theta = 60°$ shows similar level of agreement as that at $\theta = 90°$, and the spectra plotted in figure 17(c) resemble those shown in figure 14(c). Results on the other side of the plate are shown in figure 17(d-f). Due to the similarity to those discussed above, a detailed discussion seems superfluous.

It is, however, worth noting that the agreement between the model predictions and experimental observations is much better when the plate is moved slightly closer to $H = 1.5D$, as shown in figure 18. The maximum noise enhancement observed at 90° on the shielded side in the experiment matches closely to the model's prediction. Even the spectral oscillations appear to be partially predicted. Noise shielding effects for this configuration are also predicted reasonably well. The agreement at both 60° and 30° to the jet axis is similar to that described above. And it is worth mentioning again the excellent noise prediction at 90° on the reflected side.

One can further compare the results when the plate's trailing-edge is placed at $L = 4D$ and $H = 1.25D$. The fact that the spectral oscillations are partially captured is more marked. The general trend, however, largely resembles that shown in figure 18. We therefore omit a repetitive description of them.

VII. CONCLUSION

A series of experimental tests are carried out in this paper to investigate jet installation effects, together with the effects of varying H, L and the jet Mach number on installed jet noise. It is found that the plate causes jet noise to be enhanced significantly at low

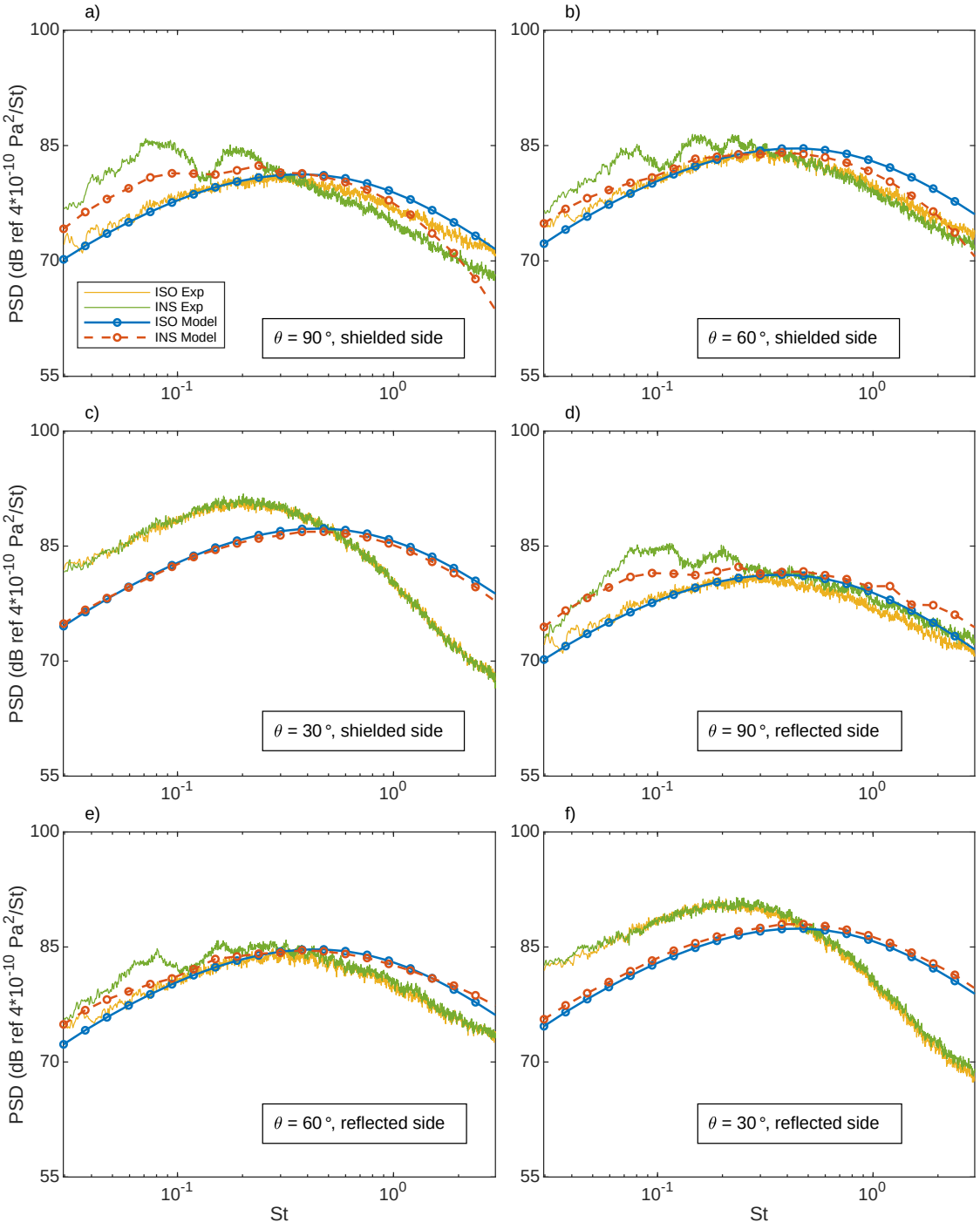

FIG. 17: Comparison of the predicted isolated and installed noise spectra with experimental results at various observer locations for $L = 4D$ and $H = 2D$.

frequencies, and jet noise is either suppressed or increased by around 3 dB at high frequencies on the shielded and reflected sides, respectively. It is demonstrated that increasing H (while L is fixed) causes the low-frequency amplification to decrease exponentially but results in little change for both the shielding and reflection effects at high frequencies. Increasing

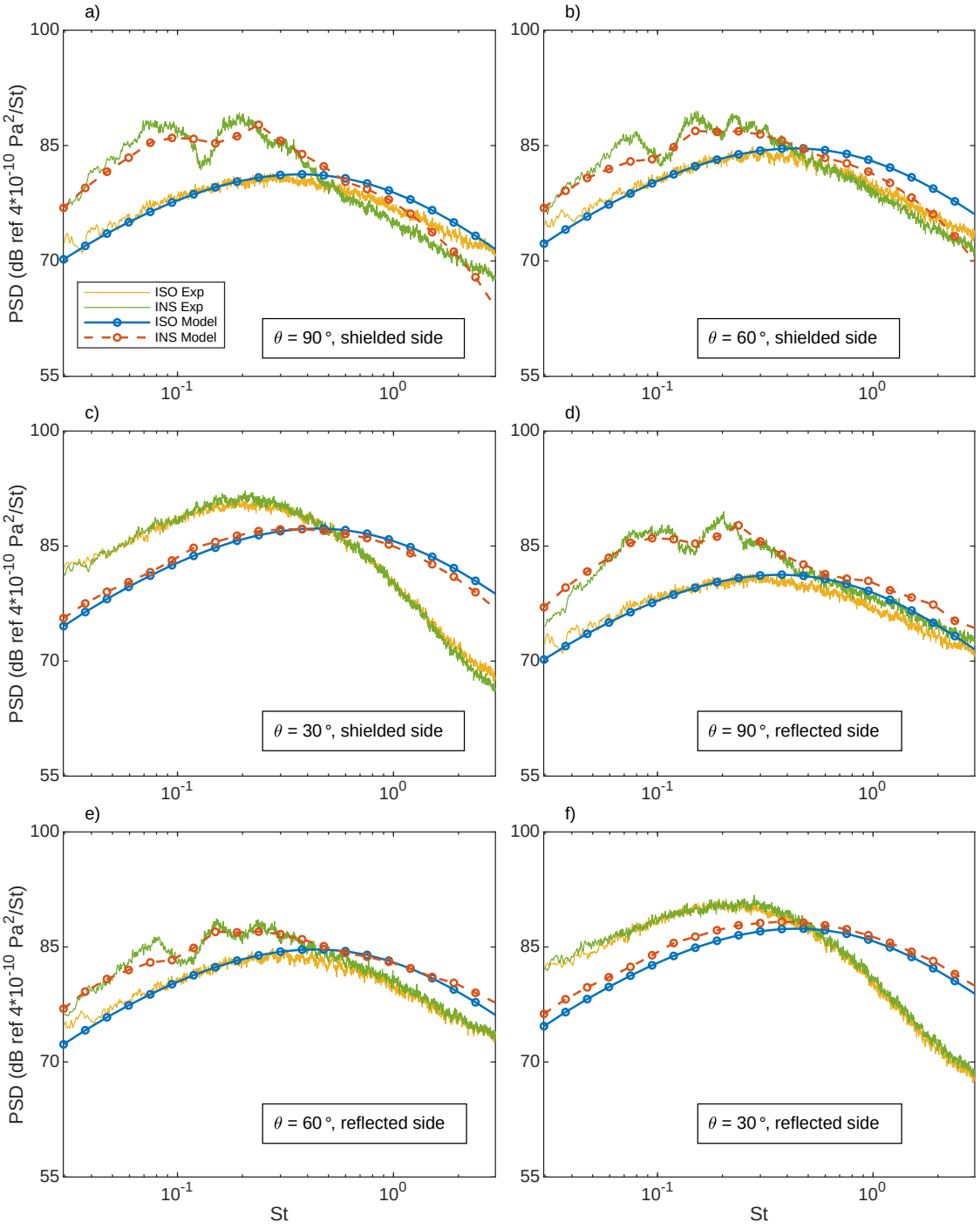

FIG. 18: Comparison of the predicted isolated and installed noise spectra with experimental results at various observer locations for $L = 4D$ and $H = 1.5D$.

L (while H is fixed), on the other hand, produces stronger noise intensification at low frequencies and slightly more effective shielding or reflection effects at high frequencies. The installation effects are found to be less pronounced as the jet Mach number increases.

The results are then compared with the predictions using the hybrid model developed

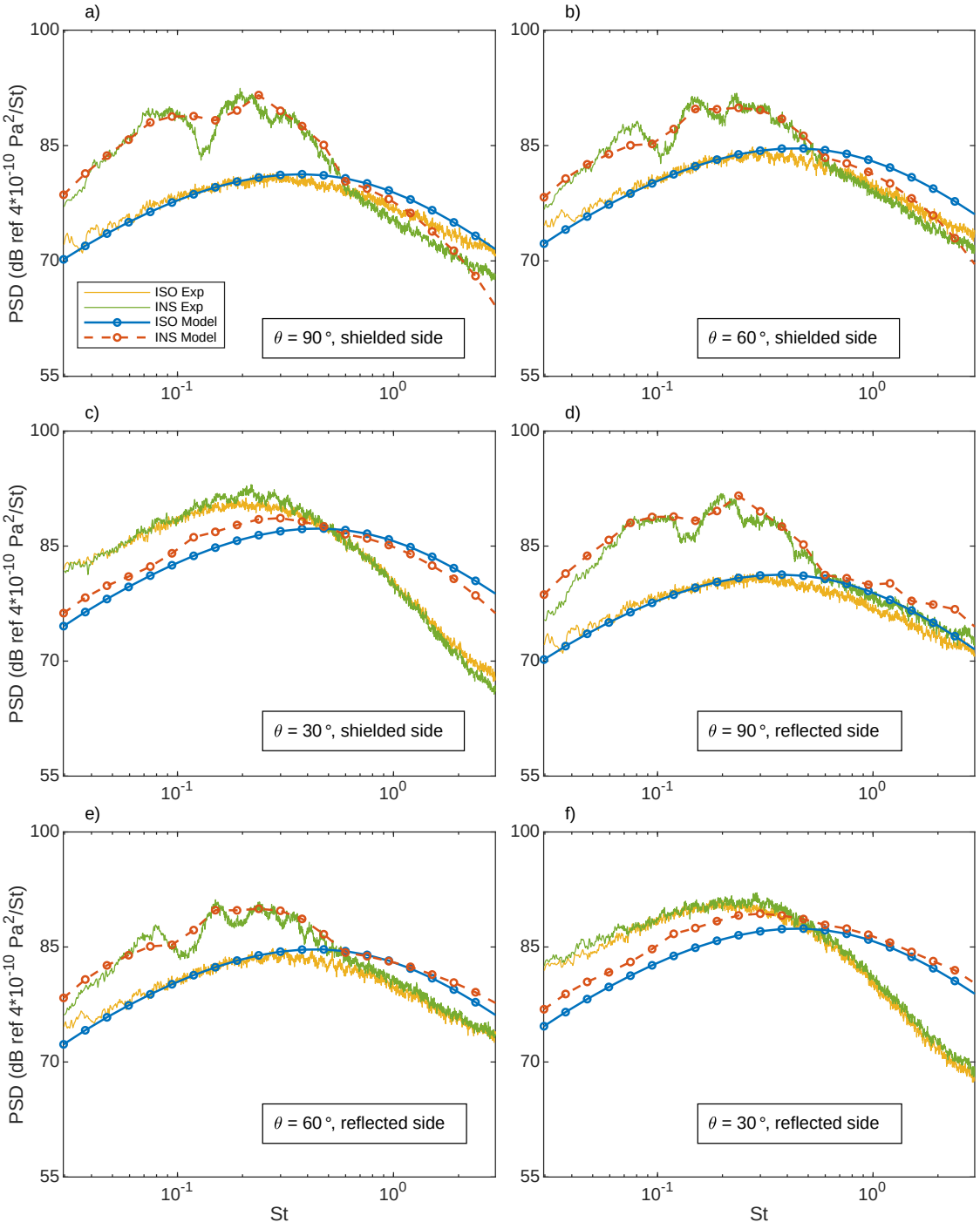

FIG. 19: Comparison of the predicted isolated and installed noise spectra with experimental results at various observer locations for $L = 4D$ and $H = 1.25D$.

in the earlier work of the authors.[23] Excellent agreement is achieved for the low-frequency noise enhancement caused by instability wave scattering when the plate is placed at different positions. This remarkable agreement shows that the near-field scattering model captures the correct noise mechanism for the low-frequency noise enhancement and provides a robust

and accurate prediction tool for the installation effects for a given isolated jet. In addition, the quadrupole-scattering model can also correctly predict the noise spectra for an observer angle of 90° on the reflected side of the flat plate. At lower observer angles, deviations occur due to the jet refraction effects. However, it can qualitatively predict both the shielding and reflection effects at high frequencies. An improved model incorporating these refraction effects will be studied in our future work. In addition, the frequency dependence of the instability waves' convection velocity in the low-frequency regime appears to be very interesting. This will be studied from a stability analysis perspective in future work.

ACKNOWLEDGMENTS

The first author (B. Lyu) wishes to gratefully acknowledge the financial support provided by the Cambridge Commonweath European and Internatinoal Trust and the China Scholarship Council.

APPENDIX

A. On the spectral oscillations

To show that the oscillations observed in the installed jet noise spectra are due to the finite chord length of the flat plate, first note that the frequencies where the oscillatory peaks and troughs appear remain unchanged when either L or H changes. This can be seen, for example, by comparing figures 15a, 16a, 18a, and 19a. This shows that the cause of such an oscillation is most likely to be related with the size of the plate, which is kept constant.

The existing literature on the turbulent boundary layer trailing-edge noise (TE noise) can be used to support such an argument quantitatively (see, for example, Amiet,[18] Roger and Moreau,[28] and Lyu, Azarpeyvand, and Sinayoko[36]). TE noise is a common issue in applications such as wind turbines and cooling fans. It refers to the noise generated when the turbulence in the boundary layer convects past and gets scattered by the sharp trailing edge of an aerofoil. Amiet's approach[18] is widely used in the aeroacoustic community to model the TE noise. Amiet's model was developed in two steps. Firstly, the aerofoil was simplified as a flat plate, and the scattered pressure on the upper and lower surfaces was calculated using the Schwarzschild method. In doing so, the leading edge of the aerofoil was often assumed to be far away from the trailing edge and hence cause minimal back scattering. The work of Roger and Moreau[28] extended Amiet's model by taking into account the leading-edge back scattering. It found that when $kc > 1$ the leading-edge back scattering is negligible. Secondly, the far-field sound was obtained by integrating the surface pressure based on the theory of Kirchhoff and Curle.[37] Hence, we can see that the finite size of the

plate was partially taken into account (no leading-edge back scattering, but the surface pressure integral domain is finite). Because the chord length is finite, one expects some oscillatory pattern in the spectrum because the surface pressure has an oscillatory pattern along the chord.[18,38] Figure 7a (black dashed line) in the work of Lyu, Azarpeyvand, and Sinayoko[36] represents a typical TE noise spectrum. The oscillatory nature is clear.

The instability-wave scattering model shown in Section II uses Amiet's approach to obtain the far-field sound. The oscillatory nature would also appear in the installed jet noise context. We can make a quantitative comparison between locations where the first trough and peak appear between the aforementioned figure and those observed in the experiment. It has been shown that the frequency where the peak or trough appears has a strong dependence on k and a weak dependence on k_1 (see Roger and Moreau,[28] and Lyu, Azarpeyvand, and Sinayoko[36]). Therefore, though the values of k_1 are different between the aforementioned Figure 7a and our experiment, we expect the peak or tough frequency to more or less match each other. The TE noise figure shows that the first dip frequency at around $kc = 5.2$ and the following peak frequency at around $kc = 8$. In the experiment $c = 12D$ and these correspond to the frequencies at 931 Hz ($St \approx 0.14$) and 1433 Hz ($St \approx 0.21$), respectively. This matches the experimental results very well. We therefore believe that this oscillatory pattern is due to the finite chord length of the flat plate.

REFERENCES

[1]K. Bushell, "Measurement and prediction of jet noise in flight," in *Proceedings of 2nd Aeroacoustics Conference*, Aeroacoustics Conferences (American Institute of Aeronautics and Astronautics, 1975) AIAA 75-461.

[2]R. Head and M. Fisher, "Jet/surface interaction noise - analysis of farfield low frequency augmentations of jet noise due to the presence of a solid shield," in *Proceedings of 3rd Aeroacoustics Conference*, Aeroacoustics Conferences (American Institute of Aeronautics and Astronautics, 1976) AIAA 76-502.

[3]V. Szewczyk, "Coaxial jet noise in flight," in *Proceedings of 5th Aeroacoustics Conference*, Aeroacoustics Conferences (American Institute of Aeronautics and Astronautics, 1979) AIAA 79-636.

[4]D. Way and B. Turner, "Model tests demonstrating under-wing installation effects on engine exhaust noise," in *Proceedings of 6th Aeroacoustics Conference*, Aeroacoustics Conferences (American Institute of Aeronautics and Astronautics, 1980) AIAA 80-1048.

[5]J. G. Shearin, "Investigation of jet-installation noise sources under static conditions," NASA Technical Report 2181 (NASA Langley Research Center, , Hampton, Virgina, 1983).

[6]R. Stevens, W. Bryce, and V. Szewczyk, "Model and full-scale studies of the exhaust noise from a bypass engine in flight," in *Proceedings of 8th Aeroacoustics Conference*,

Aeroacoustics Conferences (American Institute of Aeronautics and Astronautics, 1983) AIAA 83-751.

[7]G. Sengupta, "Analysis of jet-airframe interaction noise," in *Proceedings of 8th Aeroacoustics Conference*, Aeroacoustics Conferences (American Institute of Aeronautics and Astronautics, 1983) AIAA 83-783.

[8]M. Wang, "Wing effect on jet noise propagation," in *Proceedings of 6th Aeroacoustics Conference*, Aeroacoustics Conferences (American Institute of Aeronautics and Astronautics, 1980) AIAA 80-1047.

[9]C. Mead and P. Strange, "Under-wing installation effects on jet noise at sideline," in *Proceedings of 4th AIAA/CEAS Aeroacoustics Conference*, Aeroacoustics Conferences (American Institute of Aeronautics and Astronautics, 1998) AIAA 98-2207.

[10]T. R. S. Bhat and A. M. Blackner, "Installed jet noise prediction model for coaxial jets," in *Proceedings of 9th AIAA/CEAS Aeroacoustics Conference*, Aeroacoustics Conferences (American Institute of Aeronautics and Astronautics, 1998) AIAA 98-79.

[11]A. Moore, "A 3D prediction of the wing reflection of aero engine noise," in *Proceedings of 10th AIAA/CEAS Aeroacoustics Conference*, Aeroacoustics Conferences (American Institute of Aeronautics and Astronautics, 2004) AIAA 2004-2865.

[12]N. N. Pastouchenko and C. K. W. Tam, "Installation effects on the flow and noise of wing mounted jets," AIAA Journal **45**, 2851–2860 (2007).

[13]C. A. Brown, "Jet-surface interaction test: far-field noise results," Journal of Engineering for Gas Turbines and Power **135**, 71201 (2013).

[14]D. Papamoschou, "Prediction of jet noise shielding," in *Proceedings of the 48th AIAA Aerospace Sciences Meeting* (American Institute of Aeronautics and Astronatics, 2010) AIAA 2010-653.

[15]A. V. G. Cavalieri, P. Jordan, W. Wolf, and Y. Gervais, "Scattering of wavepackets by a flat plate in the vicinity of a turbulent jet," Journal of Sound and Vibration **333**, 6516–6531 (2014).

[16]S. Piantanida, V. Jaunet, J. Huber, W. Wolf, P. Jordan, and A. Cavalieri, "Scattering of turbulent-jet wavepackets by a swept trailing edge," Journal of the Acoustical Society of America **140**, 4350–4359 (2016).

[17]J. Vera, R. H. Self, and M. J. Kingan, "The prediction of the radiated pressure spectrum produced by jet-wing interaction," in *Proceedings of 21st AIAA/CEAS Aeroacoustic Conference*, Aeroacoustics Conferences (American Institute of Aeroacoustic and Astronautics, 2015) AIAA 2015-2216.

[18]R. K. Amiet, "Noise due to turbulent flow past a trailing edge," Journal of Sound and Vibration **47**, 387–393 (1976).

[19]S. Piantanida, V. Jaunet, J. Huber, W. Wolf, P. Jordan, and A. V. G. Cavalieri, "Scattering of turbulent-jet wavepackets by a swept trailing edge," in *Proceedings of 21st*

AIAA/CEAS Aeroacoustic Conference, Aeroacoustics Conferences (American Institute of Aeroacoustic and Astronautics, 2015) AIAA 2015-2998.

[20]P. Nogueira, A. Cavalieri, and P. Jordan, "A model problem for sound radiation by an installed jet," Journal of Sound and Vibration **391**, 95–115 (2017).

[21]L. Bastos, C. Deschamps, and A. da Silva, "Experimental investigation of the far-field noise due to jet-surface interaction combined with a chevron nozzle," Applied Acoustics **127**, 240–249 (2017).

[22]B. Lyu and A. P. Dowling, "Noise prediction for installed jets," in *Proceedings of 22nd AIAA/CEAS Aeroacoustics Conference*, Aeroacoustics Conferences (American Institute of Aeronautics and Astronautics, 2016) AIAA 2016-2986.

[23]B. Lyu, A. Dowling, and I. Naqavi, "Prediction of installed jet noise," Journal of Fluid Mechanics **811**, 234–268 (2017).

[24]S. A. Karabasov, M. Z. Afsar, T. P. Hynes, A. P. Dowling, W. A. McMullan, C. D. Pokora, G. J. Page, and J. J. McGuirk, "Jet noise: acoustic analogy informed by large eddy simulation," AIAA Journal **48**, 1312–1325 (2010).

[25]N. K. D. Mohan, A. P. Dowling, S. A. Karabasov, H. Xia, O. Graham, T. P. Hynes, and P. G. Tucker, "Acoustic sources and far-field noise of chevron and round jets," AIAA Journal **53**, 2421–2436 (2015).

[26]H. K. Tanna, "An experimental study of jet noise part I: Turbulent mixing noise," Journal of sound and Vibration **50**, 405–428 (1977).

[27]M. Bondarenko, Z. Hu, and X. Zhang, "Large-Eddy Simulation of the interaction of a jet with a wing," in *Proceedings of 18th AIAA/CEAS Aeroacoustics Conference*, Aeroacoustics Conferences (American Institute of Aeronautics and Astronautics, 2012) AIAA 2012-2254.

[28]M. Roger and S. Moreau, "Back-scattering correction and further extensions of Amiet's trailing-edge noise model. part 1: theory," Journal of Sound and Vibration **286**, 477–506 (2005).

[29]P. Jordan and T. Colonius, "Wave packets and turbulent jet noise," Annual Review of Fluid Mechanis **45**, 173–195 (2013).

[30]M. J. Lighthill, "On sound generated aerodynamically. I. General theory," Proceedings of the Royal Society A: Mathematical, Physical and Engineering Sciences **211**, 564–587 (1952).

[31]S. C. Crow and F. H. Champagne, "Orderly structure in jet turbulence," Journal of Fluid Mechanics **48**, 547–591 (1971).

[32]A. Michalke, "Instabilität eines kompressiblen runden freistrahls unter berücksichtigung des einflusses der strahlgrenzschichtdicke," Zeitschrift für Flugwissenschaften **19**, 319–328 (1971).

[33]A. Michalke, "Survey on jet instability theory," Progress in Aerospace Science **21**, 159–199 (1984).

[34]C. E. Tinney and P. Jordan, "The near pressure field of co-axial subsonic jets," Journal of Fluid Mechanics **611**, 175–204 (2008).

[35]C. E. Tinney, M. N. Glauser, and L. S. Ukeiley, "Low-dimensional characteristics of a transonic jet. part 1. proper orthogonal decomposition," Journal of Fluid Mechanics **612**, 107–141 (2008).

[36]B. Lyu, M. Azarpeyvand, and S. Sinayoko, "Noise prediction for serrated trailing edges," Journal of Fluid Mechanics **793**, 556–588 (2016).

[37]N. Curle, "The influence of solid boundaries upon aerodynamic sound," Proceedings of the Royal Society A: Mathematical, Physical and Engineering Sciences **231**, 505–514 (1955).

[38]R. K. Amiet, "Acoustic radiation from an airfoil in a turbulent stream," Journal of Sound and Vibration **41**, 407–420 (1975).